KAGRA Main Interferometer Design Document

KAGRA Main Interferometer Working Group

March 21, 2012

Contents

Chapter 1

Introduction

In this document, we will describe the design of the KAGRA interferometer. KAGRA will be developed in two phases. The first phase of KAGRA is called initial KAGRA or iKAGRA. This is a reduced version of the full configuration KAGRA, which is referred to as the baseline KAGRA or bKAGRA. The main purpose of iKAGRA is to gain experience in operating a large interferometer in the underground environment and to identify potential facility problems as early as possible. Therefore, the design of iKAGRA is derived from bKAGRA as a natural pass point to the full configuration. For this reason, we will mainly focus on design of bKAGRA interferometer. At the end of this document, the iKAGRA design is explained by pointing out the difference between the bKAGRA configuration.

1.1 Requirements

The bKAGRA interferometer has to meet the requirements listed below.

- The main interferometer has to be able to achieve the target sensitivities of bKAGRA shown in Figure 1.1 and 1.2. These target sensitivities are determined as a result of the optimization of the optical parameters given fundamental noise sources other than quantum noises. Details of the optimization work are described in [1].
- bKAGRA has two operation modes: BRSE and DRSE. The main interferer configuration should allow us to switch between the two modes within a reasonable amount of time.
- The control schemes of the KAGRA has to be robust enough to ensure stable operation of the interferometer in the environmental disturbances of Kamioka mine. The target duty cycle during the observation is more than 90%.

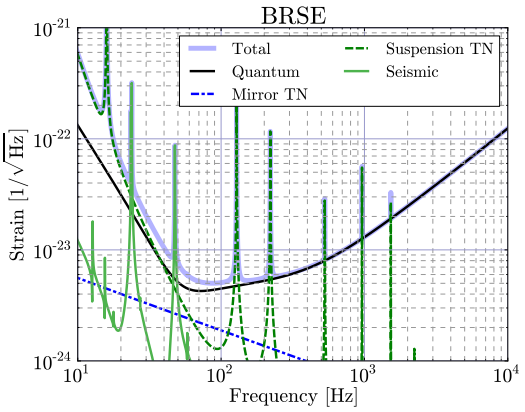

Figure 1.1: bKAGRA Target Sensitivity in the BRSE mode

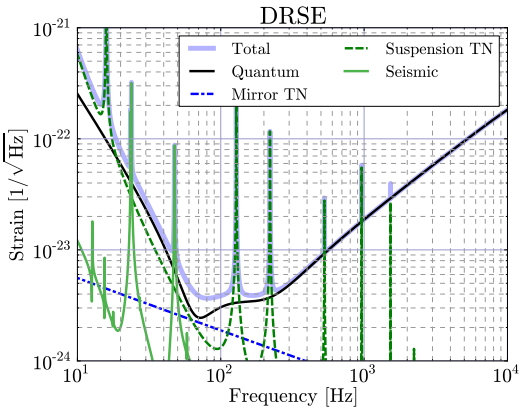

Figure 1.2: bKAGRA Target Sensitivity in the DRSE mode

Chapter 2

Optical Configuration

2.1 Overview

The main interferometer part of bKAGRA is a dual recycled Fabry-Perot Michelson interferometer operating in a resonant-sideband extraction (RSE) mode. This interferometer is designed to be operated in two modes, Broadband RSE (BRSE) and Detuned RSE (DRSE). The schematic view of the main interferometer and the naming convention of the interferometer components are shown in Figure 2.1.

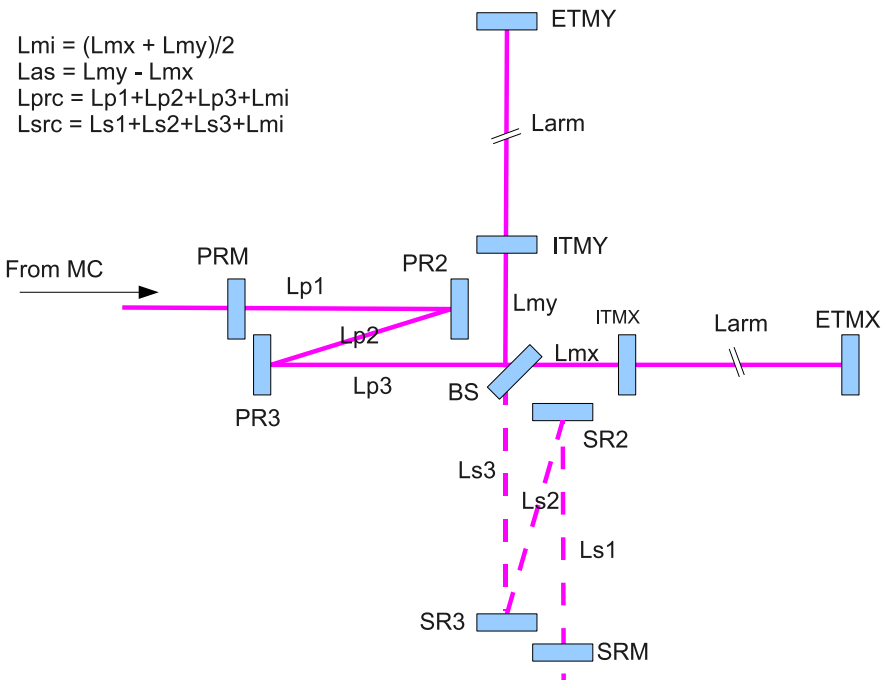

Figure 2.1: Schematic of the main interferometer and the naming convention of IFO parameters

Parameter Name	Value	Comments
Arm cavity length	3000.00 m	
ITM Reflectivity	99.6%	
ITM Radius of Curvature	1680(±8) m	
ITM Beam Size	3.5 cm	$1/e^2$ radius
ETM Reflectivity	>99.9945%	
ETM Radius of Curvature	1870(±9) m	
ETM Beam Size	4.0 cm	$1/e^2$ radius
g-factor	0.473	$g_1 \cdot g_2$
Round Trip Loss	<100 ppm	
Finesse	1530	

Table 2.1: Arm cavity parameters

2.2 Arm Cavity Parameters

The arm cavity (AC) parameters are summarized in Table 2.1. The arm cavity length is constrained to less than 3 km by the size of the mountain. So we chose the largest one. The finesse of the arm cavities is about 1500. This rather high finesse is chosen to avoid high optical power from transmitting through ITMs, thus reducing the heat generation in the mirror [1]. This is critical to meet the cooling capacity of the cryocoolers. From the finesse, the reflectivities of the mirrors are determined. The round trip loss of the cavity including the ETM transmission should be less than 100 ppm. As more concrete requirements, we assign 10 ppm to the transmission and 45 ppm each to the reflection loss of each mirror.

g-factor

The radius of curvature of the mirrors are selected to realize the desirable beam spot sizes on the mirrors. From the point of view of the thermal noise, we want to make the spot size as large as possible. Considering the size of the mirror (22 cm diameter) and requiring the diffraction loss per reflection to be less than 1 ppm, the largest possible beam radius is 4.0 cm. We employ this number as the ETM spot size. For the ITMs, the dielectric coating is thinner because of the smaller reflectivity. Thus, the impact on the sensitivity is minimal, even if we reduce the beam size on the ITMs to 3.5 cm (the reduction of the sensitivity in terms of the inspiral range by this change is about 2Mpc [2]). A smaller beam in the vertex makes it easier to handle the stray beams in the congested BS chamber. Therefore, we decided to set the beam size on the ITMs to be 3.5 cm.

There are two possible choices of mirror curvatures to realize the same spot sizes. The first set of the ROCs is ITM=14km and ETM=7.5km, which gives positive g-factors, g1=0.786 and g2=0.602. Another possibility is ITM=1.68km and ETM=1.87km, corresponding to negative g-factors, g1=-0.786 and g2=-0.602. In order to decide the polarity of the g-factors, we considered the higher order mode (HOM) resonances, parametric instability and the angular optical spring instability.

2.2.1 Arm Cavity Higher Order Mode Resonances

Ideally, the arm cavities should resonate only the TEM00 mode. However, optical higher modes are not completely anti-resonant to the AC in general. Therefore, if there is mis-alignment or mode mis-matching, HOMs could resonate in the AC, potentially increasing the shot noise. If the selected arm g-factor is a particularly bad one, this HOM coupling could be large. In this section, we will check if

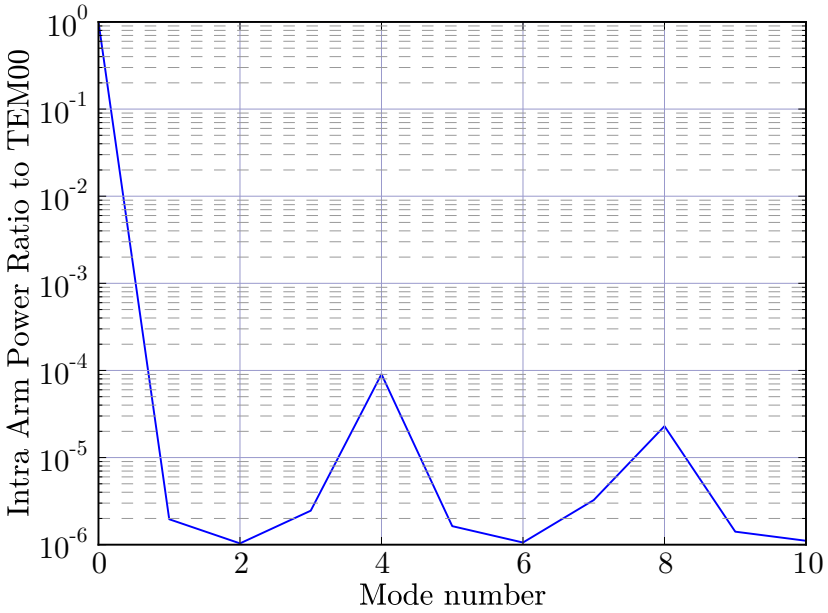

Figure 2.2: HOM power in the arm cavity relative to the TEM00 power. The mode number is defined as $n + m$ for TEMnm modes.

our arm cavity design is robust against this problem. We will compare the two cases of g-factors, the negative one and the positive one.

Figure 2.2 shows the HOM power ratio to the TEM00 power in the AC. This is the ratio of the intra-cavity optical power, if TEM00 and TEMnm modes are injected to the AC with the same power. Of course, it is very unlikely, thus in reality, the ratio is much smaller.

When calculating the HOM power, we took into account the fact that for HOMs, the diffraction loss is higher than TEM00. This is because HOMs are spatially spread more widely. Figure 2.3 shows the resonance curves of various HOMs. The power build up is suppressed quickly as the mode number gets higher. These curves are calculated using SIS[ref].

Figure 2.2 assumed that the g-factor of the cavity is exactly as designed. In reality, there is always some error in the ROC of the real mirrors. We set the error tolerance to be $\pm 0.5\%$ mainly from the technical feasibility of the mirror polishing. Figure 2.4 and Figure 2.5 show the maximum HOM power ratio (the value of the highest peak in Figure 2.2 except for the mode number = 0) as a function of ITM ROC error and ETM ROC error. The ROCs are swept by $\pm 1\%$ of the nominal values. These figures are for the negative g-factor case. Figure 2.6 and Figure 2.7 show the same plots for the positive g-factor case. In both the cases, the HOM power does not go up so much within the tolerated ROC errors.

g-factor

By comparing the dependence of the HOM resonance in the AC on the mirror ROC errors between the negative and positive g-factor cases, there is no significant difference between them. Therefore, both g-factors are acceptable from the point of view of this problem.

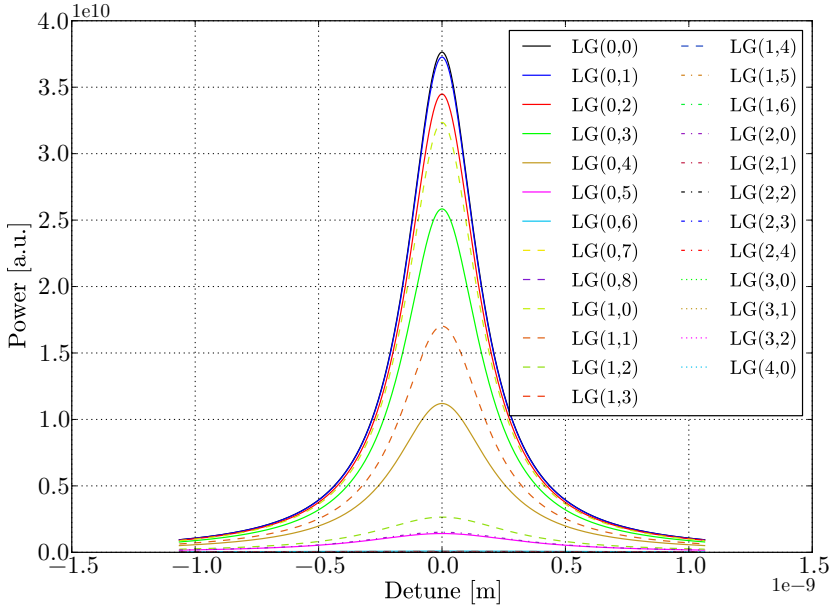

Figure 2.3: Resonance curves of HOMs taking into account the diffraction loss. The HOMs are expanded by the Laguerre-Gaussian basis. LG(p, l) corresponds to the mode number $2p + l$.

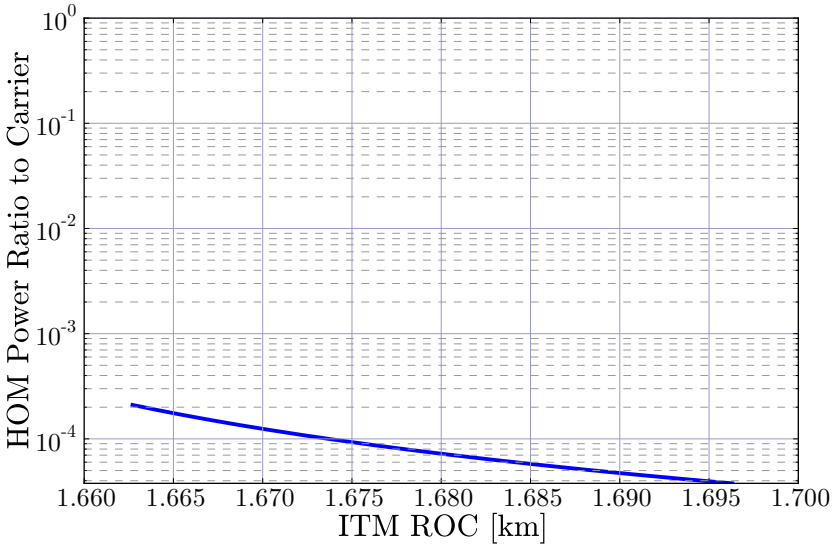

Figure 2.4: The maximum HOM power ratio in the AC as a function of ITM ROC error for the negative g-factors. The ROC is swept by ±1% around the nominal value.

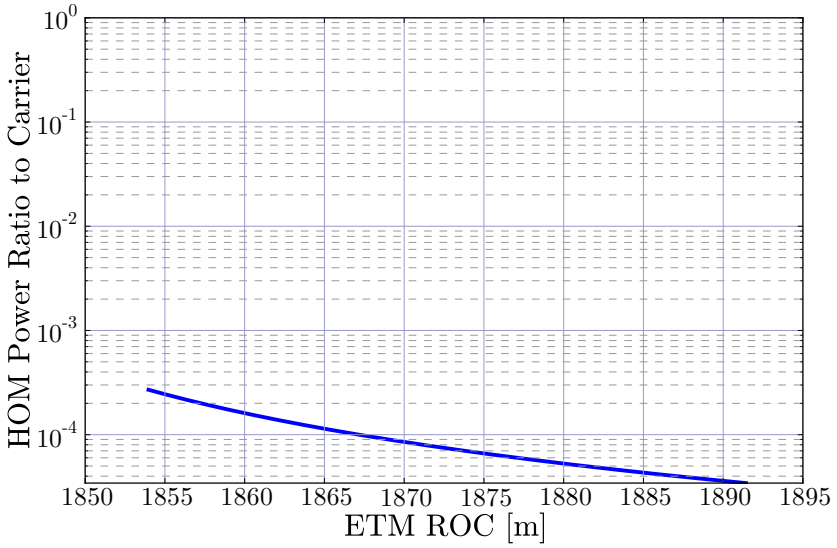

Figure 2.5: The maximum HOM power ratio in the AC as a function of ETM ROC error for the positive g-factors. The ROC is swept by ±1% around the nominal value.

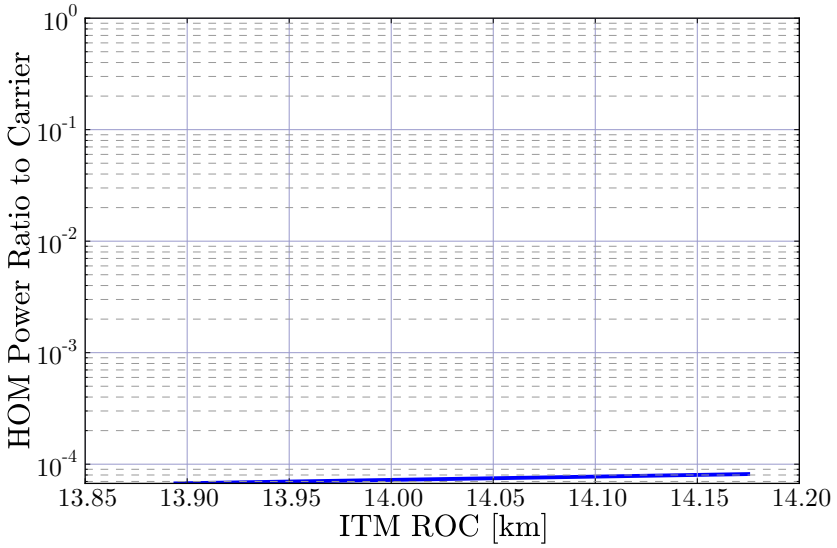

Figure 2.6: The maximum HOM power ratio in the AC as a function of ITM ROC error for the positive g-factors. The ROC is swept by ±1% around the nominal value.

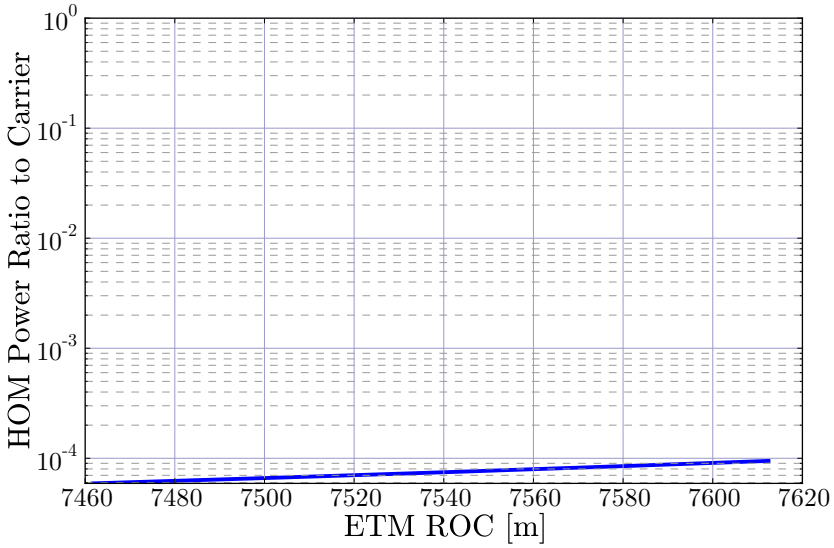

Figure 2.7: The maximum HOM power ratio in the AC as a function of ETM ROC error for the positive g-factors. The ROC is swept by ±1% around the nominal value.

2.2.2 RF Sidebands Resonances in the Arm Cavities

Fine Adjustment of the RF Sideband Frequencies

As explained in section 3, we will use three RF sidebands (RF SBs), namely f1, f2 and f3, to extract the error signals for the interferometer control. We also want to prevent the RF sidebands including their HOMs from accidentally resonating in the arm cavities. The f3 sideband is not resonant in the PRC, so it does not see the arm cavities at all. Therefore, we only consider f1 and f3 sidebands in this section.

Before proceeding to check the HOM resonances of the RF sidebands, there is a subtle but important point to note about the fine adjustment of the sideband frequencies. The RF sidebands f1 and f2 are almost anti-resonant to the arm cavities but not perfectly so. A consequence of this is that they get finite phase shifts when reflected by the ACs. Those two sidebands are supposed to resonate in the PRC at the same time. However, if the phase shifts they get from the AC are arbitrary, the resonant conditions for them is different, thus not being able to resonate both at the same time. A solution to this problem is the following: The effective length change caused by a phase shift ϕ for a modulation sideband with the modulation frequency ω_{m} is $\Delta L = \phi c/\omega_{\mathrm{m}}$. Therefore, if the phase shifts for the f1 and f2 SBs are proportional to their frequencies, the effective length change is the same for the two SBs. Then we can just pre-shorten the PRC length by this amount to fulfill the resonant conditions for both the SBs at the same time.

In order to adjust the reflection phases for f1 and f2, we need to change their frequencies. However, as explained in section 3, the ratio of f1 and f2 frequencies has to be 3:8. Therefore, we can only change the frequencies under the constraint of keeping the ratio unchanged. This condition is automatically satisfied by requiring the two sidebands to transmit the MC. That is, the f1 frequency is 3 times the FSR of MC and f2 is 8 times the MC FSR. Therefore, we will slightly change the MC length from its nominal value to find the optimal RF SB frequencies which give the AC reflection phases proportional to them. The precise amount of phase shifts induced on nearly-anti-resonant fields depends on the finesse of the cavity. Therefore, the RFSB frequencies must be adjusted according to the measurement of the real arm cavities. In the design phase, we assume 100 ppm of loss in the arm, resulting in the finesse

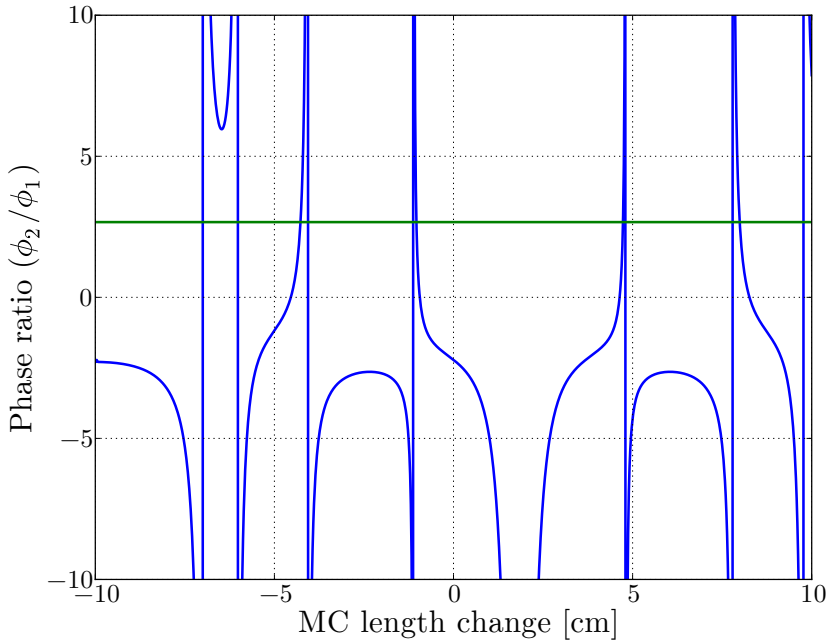

Figure 2.8: Ratio of the SB reflection phases by the arm cavities. We want to set it to 8/3, which is indicated by the green line.

of 1530. Figure 2.8 shows the ratio of the reflection phases (ϕ_2/ϕ_1) as a function of the MC length. The desired value of 8/3 is indicated by the green horizontal line. By finding a intersection of the blue curve with the green line, the tentative numbers for the RFSB frequencies are, f1=16.881 MHz and f2=45.016 MHz. However, again, these numbers should be corrected based on the finesse measurements of the actual arm cavities. Figure 2.9 shows the relative positions of the RFSBs in the FSR of the arm cavities.

HOM Resonances of the RF Sidebands

Once the exact frequencies of the RF SBs are determined, we can check the resonant conditions of the RF SBs and their HOMs in the arm cavities. Figure 2.9 shows the positions of the RF SBs and the HOMs in the FSR of the arm cavity. In the figure, both the HOM resonant curves (Lorentzian-shaped curves with mode numbers) and the harmonics of the RF SBs (vertical lines: black for f1, red for f2). If a vertical line overlaps well with one of the HOM resonances, then this RF SB harmonics may resonate in the ACs when the cavity is mis-aligned and the HOM is excited. If it happens to the first harmonics of the RF SBs, which are used for the signal extraction, the error signals will be disturbed and in the worst case we will lose the interferometer lock. Higher order harmonics are not so important, but still some of them contribute to the error signal through inter-modulations with other higher order harmonics. Therefore it is better to avoid overlaps as much as possible.

In order to see how the overlap between the RF SB harmonics and the HOM resonances changes as the ROC of the mirrors, we use a figure of merit for the overlap defined as follows: For all combinations of an RF SB harmonics and a HOM, the intra-cavity power is calculated assuming that the SB is 100% in this HOM. The diffraction loss of Figure 2.3 is taken into account. Then we take the power ratio between this calculated power to the TEM00 power in the cavity. The FOM is the maximum of this

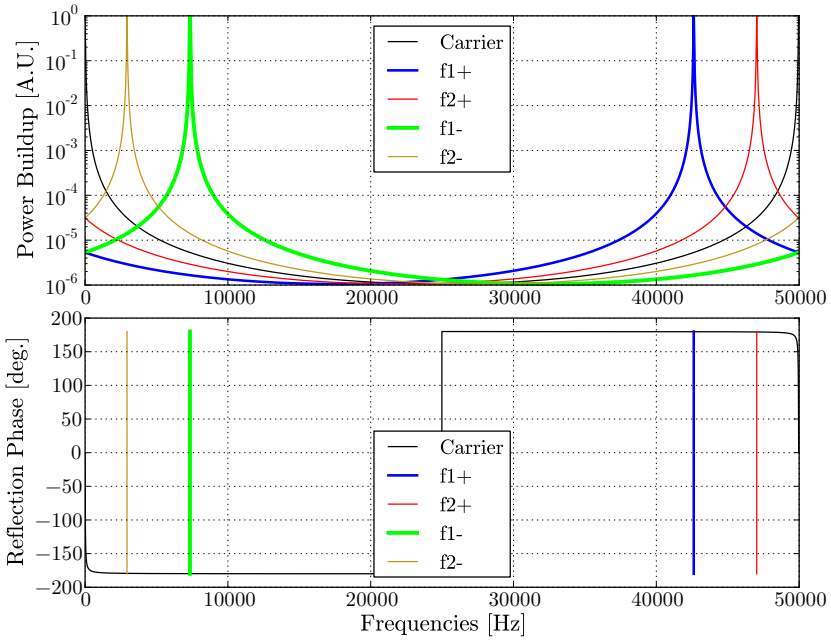

Figure 2.9: Relative position of the RFSBs in the FSR of the arm cavities.

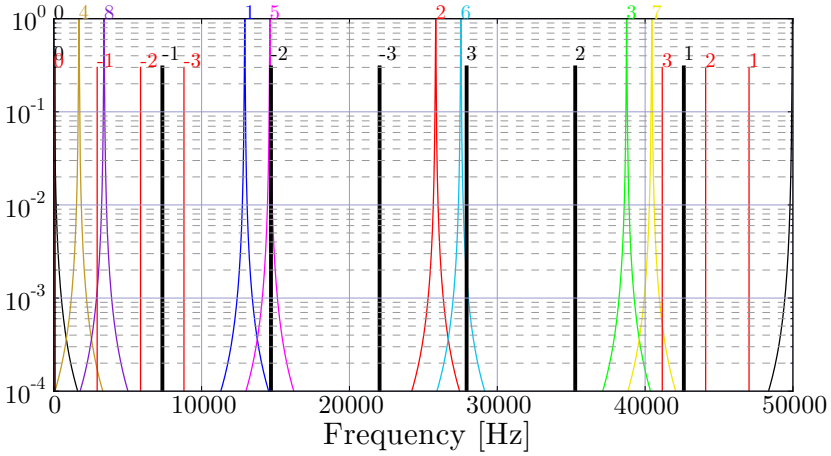

Figure 2.10: Positions of the RF SBs and the HOMs in the FSR of the arm cavities. The colorful sharp peaks represent the resonant curves of the HOMs. The mode number is printed at the top of each resonance. The vertical lines are the positions of the RF SBs and their harmonics. The numbers associated with the lines indicate the harmonic order. The black lines are the f1 harmonics, whereas the red lines are the f2 harmonics.

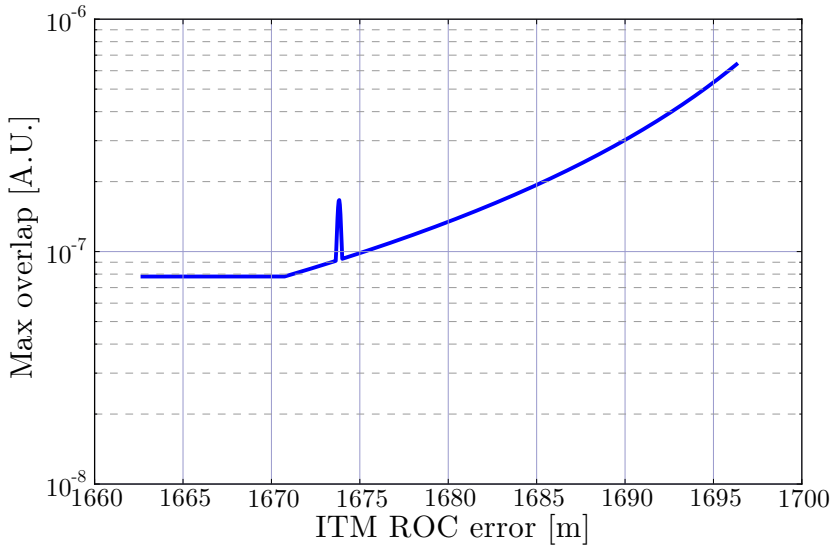

Figure 2.11: Figure of merit of the overlap between the RF SB harmonics and the HOMs when the ITM ROC is swept. g-factor is negative.

ratio from all the combinations of the RF SB harmonics and the HOMs. Figure 2.11, 2.12, 2.13 and 2.14 show the FOM as a function of ROC errors, ranging, again, ±1% of the nominal values.

Note that the meaning of the FOM above is not so clear, in a sense that there is no definite threshold below which the overlap problem is considered safe. A thorough simulation study may give some quantitative interpretation of the FOM, but we haven't done it yet. So what we can say from the above mentioned plots is just that the severity of the overlap does not change much within the specified error range of the ROCs.

g-factor and the RF SB resonances

By comparing the dependence of the RF SB resonance in the AC on the mirror ROC errors between the negative and positive g-factor cases, there is no significant difference between them. Therefore, both g-factors are acceptable from the point of view of this problem.

2.2.3 Parametric Instability

The parametric instability (PI) happens when the shape of an optical higher order mode in the arm cavity is similar to an elastic mode of the mirror substrate. In addition, the HOM's resonant frequency offset from the TEM00 must be very close to the elastic mode's eigen-frequency. The offset frequencies of the HOMs depend on the g-factor. Therefore, there are hot spots of g-factor, where PI is large.

The magnitude of the PI is characterized by the parametric gain R [3]. R is associated with each elastic mode of the mirrors. If there is a mode with R of greater than 1, this mode is unstable. We want to select a g-factor, with which no unstable mode appears.

Figure 2.15 shows the parametric gain R as a function of the ROCs of ITM and ETM. The ROCs are swept by ±2% of the nominal values. The colored areas are where R is greater than 1. Details on how to generate these plots are explained in .

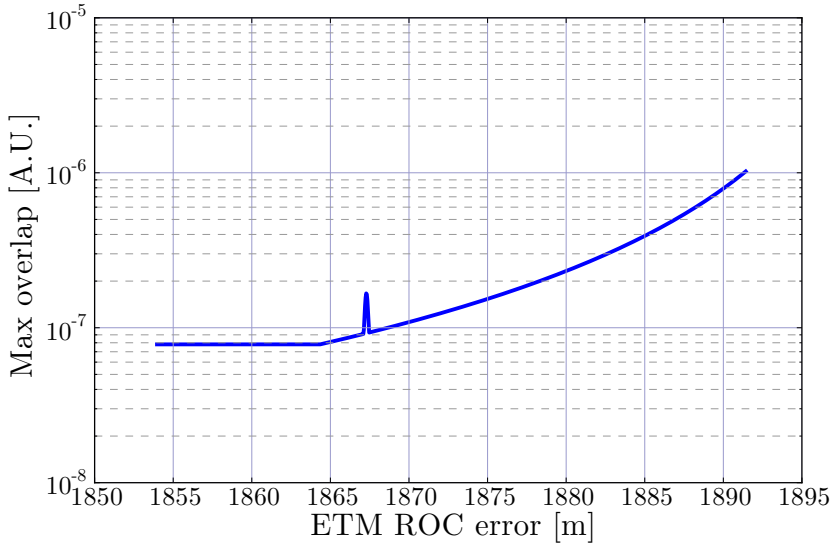

Figure 2.12: Figure of merit of the overlap between the RF SB harmonics and the HOMs when the ETM ROC is swept. g-factor is negative.

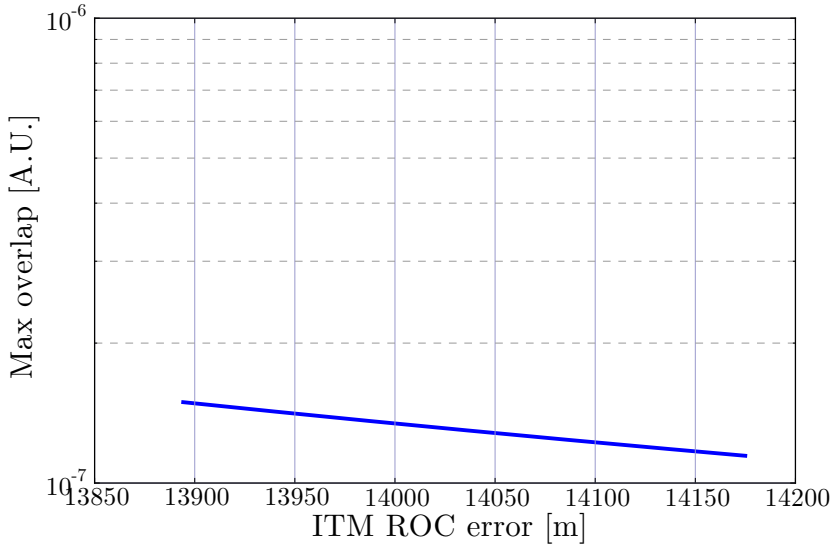

Figure 2.13: Figure of merit of the overlap between the RF SB harmonics and the HOMs when the ITM ROC is swept. g-factor is positive.

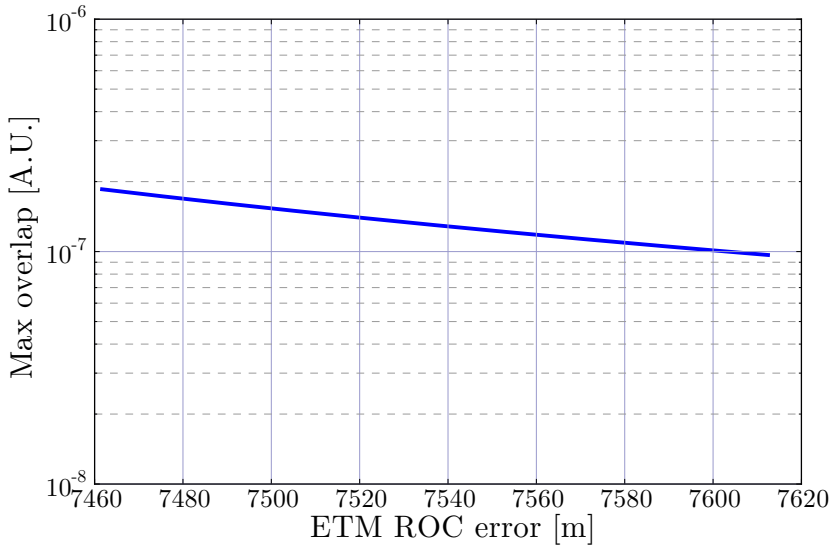

Figure 2.14: Figure of merit of the overlap between the RF SB harmonics and the HOMs when the ETM ROC is swept. g-factor is positive.

By comparing the plots for the negative and positive g-factors, there is no significant difference. The most important conclusion drawn from the plots is that there is no continuous white area which is large enough to accommodate the ±0.5% error of the ROCs. Moreover, the accuracy of the plots is not so good, because of the limited accuracy of the finite element analysis (using COMSOL). This means we cannot target a particular g-factor, even if we ignore the manufacturing error, to put our interferometer at a sweet spot (white area). In the actual interferometer, what seemed to be a sweet spot in calculation may not be a sweet spot. Therefore, regardless of the polarity of the g-factors, we have to be prepared for the PI to happen.

Once PI happens, we have to damp the oscillation somehow. Mainly two types of schemes are proposed to mitigate the PI. One is to put some lossy stuff on the side of the mirrors to damp the unstable modes. Another scheme is basically an active damping of the unstable mode using the interferometer output as an error signal. Detailed design of KAGRA PI damper is yet to be discussed.

2.2.4 Angular Instability by the Radiation Pressure

The opto-mechanical coupling between the high power optical fields circulating in the arm cavities and the mirrors create an angular optical spring effect [5]. For single cavity, there are always two eigen modes of the angular motions of the mirrors. Out of the two, one mode has a positive spring constant, meaning that the optical spring generates a restoring force. The other has a negative spring constant, potentially leading to an instability.

In general, the absolute values of the two spring constants are different. If the g-factors are negative, the negative spring constant is always smaller than the positive one. For positive g-factors, the order is the other way around. Therefore, in order to minimize this instability, negative g-factors is preferable. More quantitative comparison of the positive and negative g-factors is presented in section 5.

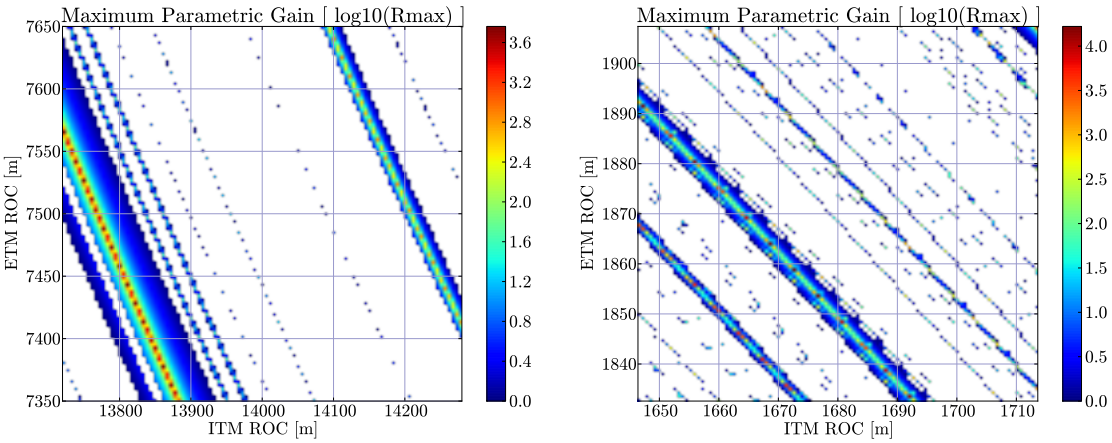

Positive g-factors

Negative g-factors

Figure 2.15: Maps of the maximum parametric gain as functions of the ROCs of the test masses. Left: positive g-factor, Right: negative g-factor. The ROCs are swept by ±2% of their nominal values. White areas correspond to $R_{\max} < 1$.

2.2.5 Conclusion on g-factors

Based on the discussions in the above few sections, we decided to select the negative g-factors, g1=-0.786 and g2=-0.602, as the design of the KAGRA arm cavities. The main reason for this selection is the radiation pressure induced angular instability.

The required ROCs to realize the positive and negative g-factors are different (R1=14km and R2=7.5km for positive, R1=1.68km and R2=1.87km for negative). Which set of ROCs is easier to manufacture is an important question to be answered. So far, we received contradictory answers from different companies: one said larger ROCs are easier to do, while another say the opposite. Therefore, the manufacturability is put out of scope of this document. It shall be addressed by the mirror group and feedback shall be given to us, the MIF group.

2.3 Recycling Cavities

Overview

There are two recycling cavities (RCs) in the KAGRA interferometer: Power Recycling Cavity (PRC) and Signal Recycling Cavity (SRC). These cavities are folded in a Z-shape by two telescope mirrors to accumulate extra Gouy phase. This is necessary to isolate the HOMs in the cavities, i.e. to stabilize the cavities in terms of the spatial modes.

The parameters of the recycling cavities are listed in Table 2.2.

2.3.1 Reflectivities

The reflectivities of the PRM and SRM are determined as a part to optimize the quantum noise shape of the interferometer [1].

Parameter Name	Value	Comments
Power Recycling Cavity Length	66.591 m	
Signal Recycling Cavity Length	66.591 m	
Michelson Average Length	25.0 m	
Michelson Asymmetry	3.330 m	
PRM Reflectivity	90%	
PRM ROC	303.96 m	
PRM Beam Size	4.03 mm	$1/e^2$ radius
PR2 ROC	-2.7628 m	
PR2 Beam Size	4.03 mm	$1/e^2$ radius
PR3 ROC	24.574 m	
PR3 Beam Size	36.479 mm	$1/e^2$ radius
PRM Reflectivity	85%	
SRM ROC	303.96 m	
SRM Beam Size	4.03 mm	$1/e^2$ radius
SR2 ROC	-2.7764 m	
SR2 Beam Size	4.03 mm	$1/e^2$ radius
SR3 ROC	24.584 m	
SR3 Beam Size	36.327 mm	$1/e^2$ radius

Table 2.2: Recycling cavity parameters

Parameter Name	Value	Comments
Lp1	14.761 m	Distance between PRM and PR2
Lp2	11.0669 m	Distance between PR2 and PR3
Lp3	15.7638 m	Distance between PR3 and BS
Ls1	14.761 m	Distance between SRM and SR2
Ls2	11.0669 m	Distance between SR2 and SR3
Ls3	15.7638 m	Distance between SR3 and BS
Folding Angle	0.6293 deg	The incident angle to the folding mirrors.

Table 2.3: Folding parameters. See Figure 2.1 for the meaning of the parameters.

2.3.2 Length and RF SB frequencies

The length parameters of the recycling cavities (RCs) are selected to resonate the RF sidebands used for the control signal extraction, which is explained in section 3. There are two RF sidebands entering the power recycling cavity (PRC), called f1 and f2. The Schnupp asymmetry of the Michelson part (MICH) is chosen to perfectly reflect the f2 sideband by MICH, so that f2 does not see the signal recycling cavity (SRC). The f1 sideband transmits through MICH and resonates in the compound cavity formed by PRC and SRC through MICH. Another sideband, called f3, will be used during the lock acquisition. It is not resonant in any part of the interferometer, thus reflected directly back by the PRM. The RF SB resonant conditions are depicted in Figure 3.1.

Constraints

While there are many possible combinations of the RC lengths and the RF SB frequencies to satisfy the above mentioned resonant conditions, we have to meet several practical constraints. First of all, the RCs cannot be too long for the obvious reason of limited space in the mine. From this point of view, the shorter the better. At the same time, the RCs cannot be too short. One reason for this is that we have to accomodate 20 m long cold segments of vacuum pipes between the BS and the ITMs. This is necessary to reduce the thermal radiation impinging on the cryogenic ITMs. Another reason is that we need some length to fold the RCs. If the RCs are short, the folding angles have to be wide. This will increase the astigmatism because the folding mirrors have curvature. For those reasons, we want the RC lengths to be about 70 m.

The next constraint is the range of the RF SB frequencies. We want them to be moderate, meaning roughly in the range of 10 MHz to 50 MHz. In this frequency range, we can find PDs with reasonable apperture size ($\sim$1 mm). If the frequency is much higher than 50 MHz, we have to use smaller PDs, which is more susceptible to beam jitter, and may take less power. If the frequency is too low, the laser noise may be larger at the demodulation frequencies. Especially, we doubt that the intensity noise is at the shot noise level in less than 10 MHz.

The two RF SBs have to transmit the mode cleaner (MC). Therefore, the FSR of the MC has to be a common measure of f_1 and f_2. The FSR, in turn determines the length of MC, as $L_{\rm MC} = c/(2f_{\rm FSR})$. In order to keep the MC length in the reasonable range (order of 30 m), the FSR cannot be too small. This sets a severe constraint on the choice of the RF SB frequencies.

SRCL linear range

We explored all possible combinations of the RC lengths and RF SB frequencies by the algorithm explained in A. After the extensive search, there are still many sets of parameters, which satisfy the above mentioned constraints. In order to determine the final parameter set, we look at the linear range of the SRCL error signal. Since we will detune the SRC by adding an offset to the error signal, the error signal has to have a reasonable slope at the detuned operation point. This situation is shown in Figure 2.16. In the plot, the SRCL error signals are plotted as functions of SRCL detuning in terms of the one-way phase change. There are three curves corresponding to different finesse of the PRC-SRC coupled cavity. The blue curve is the one with the final parameter set we selected. At the center, corresponding to the BRSE operation point, the blue curve has some slope. At the SRC detuning = 3.5 degrees, corresponding to the DRSE operation point and indicated by the black vertical line, the curve still has some slope, though it is more gradual. On the other hand, the red curve has almost zero slope at the DRSE operation point. Therefore, we cannot use this signal for controlling the SRC in DRSE. The green curve has almost constant slope, but it is less steep than the blue curve, at least at the BRSE operation point, meaning that the signal is weaker. Therefore, we prefer the blue curve.

The linear range of the SRCL error signal is roughly determined by the finesse of the PRC-SRC coupled cavity for the f1 sideband. Since the reflectivities of the PRM and the SRM are already

determined by the optimization of the quantum noise shape, we are left with the Michelson reflectivity for the f1 sideband to change the finesse of the coupled cavity.

The Michelson reflectivity $R_{\rm m}$ depends on the f1 frequency (f_1) and the Michelson asymmetry ($l_{\rm m}$) as $R_{\rm m} \propto \cos(2\pi f_1 \cdot l_{\rm m}/c)$, where c is the speed of light. When $R_{\rm m}$ is closer to the PRM reflectivity (0.9), the effective reflectivity of the power-recycled Michelson seen from the SRC becomes lower. Therefore, the finesse of the SRC gets smaller, resulting in a wider linear range.

Even though the blue curve in Figure 2.16 has a finite slope at the DRSE operation point, the second derivative is non-zero there, i.e. the error signal is non-linear. This may non-linearity could produce up- and down-conversions of error signals. This problem is examined in the appendix B. The conclusion is that this effect is small enough to worry about.

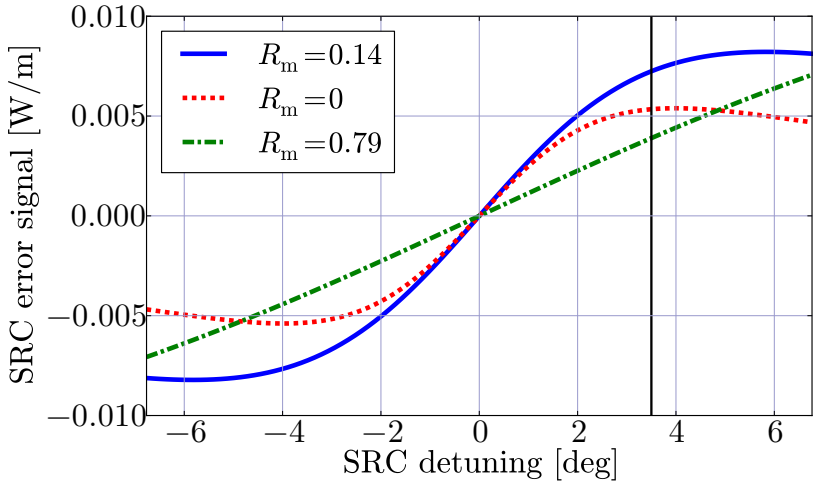

Figure 2.16: SRCL error signals for three different values of $R_{\rm m}$. The horizontal axis is the detuning of the SRC in terms of the one-way phase shift. The vertical axis is the signal from the POP port demodulated at the f1 frequency. The vertical line shows the operation point of DRSE (3.5°).

Selected Length and Frequencies

The PRC length ($L_{\rm prc}$) is set so that $f_1 = 7.5 \times F_{\rm prc}$, where $F_{\rm prc} \equiv c/(2L_{\rm prc})$ is the FSR of the PRC. Since the carrier is anti-resonant to the PRC cavity itself[1], this condition makes the round trip phase change of the f1 sideband in the PRC an integral multiple of 2π. The reflectivity of the Michelson part for f1 is 0.383 (amplitude reflectivity). Therefore, f1 transmits through MICH and reaches SRM. The SRC length ($L_{\rm src}$) is the same as $L_{\rm prc}$, thus satisfying $f_1 = 7.5 \times F_{\rm src}$. In this case, the SRC length is controlled to resonate the carrier. Therefore, SRC is anti-resonant for f1 by itself. However, there is always a $\pi/2$ phase shift associated with the transmission of MICH. During the round trip of the PRC-SRC coupled cavity, f1 experiences this phase shift twice amounting to a sign flip. Therefore, in total, the round trip phase shift of the coupled cavity is an integral multiple of 2π.

For the f2 sideband, the MICH reflectivity is -1. The FSR of PRC satisfies $f_2 = 20 \times F_{\rm prc}$. Combined with the fact that the carrier is anti-resonant and the MICH reflection induces a sign flip, f2 is resonant in the PRC. Since it is perfectly reflected by MICH, the f2 sideband does not resonate in SRC.

[1]Because the carrier gets extra phase shift of π from the arm cavities.

The average length of MICH (the average distance between BS and ITMs) is set to 25 m. Out of this 25 m, 20 m is used for the cryogenic radiation shield. The remaining 5 m is used to absorb the Schnupp asymmetry.

As explained in section 2.2.2, the two RF SBs get finite phase shifts as reflected by the ACs. Since we fine adjusted the frequencies of f1 and f2, the effective length changes by these phase shifts are the same for both of them. Thus, what we have to do is to change the PRC length (Lprc) and SRC length (Lsrc) by $dL = c\phi_1/(4\pi f_1) = c\phi_2/(4\pi f_2)$, where $\phi_{\rm x}$ and $\omega_{\rm x}$ are the phase shift and the angular frequency of the f1 or f2 sidebands.

2.3.3 Radius of Curvature of the RC mirrors

The recycling cavities are both folded by two additional mirrors to allow focusing of the beam inside the cavities. This configuration makes the recycling cavities stable in terms of spatial modes. However, the recycling cavities cannot be too stable, because then TEM10 or TEM01 modes generated by the misalignment of the arm cavities will be suppressed in the RCs. Those higher order modes are necessary for the alignment sensing by the wavefront sensing (WFS) scheme. Therefore, we need a moderately stable RCs, which reject HOMs but not completely. The one-way Gouy phase change of the TEM00 beam resonating in the RCs is selected to be 20 degrees as a compromise between the stability of the RCs and the WFS signal strength.

The ROCs of the folding mirrors are set to realize the desired Gouy phase shift. There are many combinations of the ROCs to achieve this. We selected a design which works as a beam reducing telescope. In this design, the beam coming back from the arm cavities, having the beam radius of 3.5 cm, is focused by the concave PR3 mirror down to 4 mm on the PR2. Then the convex PR2 collimates the beam, to have the same beam size on the PRM. This design is very convenient because we do not have to handle large beams at the reflection (REFL) port and the POP[2] port, which is the beam transmited through the PR2. 4 mm beams can directly taken in and out of the vacuum chambers without using large optical windows, which are expensive and tend to be fragile.

The geometry of the folding part is mainly determined by the constraints from the vacuum system, such as the minimum separation between vacuum chambers. In order to minimize the astigmatism, we chose a configuration which minimizes the folding angle under the constraints. The beam from PR3 to BS has a large radius (3.5 cm). Therefore, PR2 has to be located far enough from the beam to avoid beam clipping. On the other hand, we want to put PR2 as close to the beam as possible to minimize the astigmatism. As a result, we located the edge of PR2 at 4 times the beam radius away from the beam.

2.4 Output Mode Cleaner

An output mode cleaner (OMC) is used to filter out unwanted RF SBs and HOMs from the AS beam, so that the shot noise of the DC readout is not compromised. The OMC has to be design to reduce the RF SBs and the HOMs well bellow the local oscillator field of the DC readout. For a good rejection ratio, a high finesse cavity is preferable. However, the transimssivity of such a cavity is susceptible to the mirror losses. If the transmissivity is low, the GW signal sidebands are reduced and the SNR is degraded. Therefore, we have to strike a balance in the design of the OMC.

Detailed design of the OMC has not yet finalized. A conceptual design is discussed in [6].

[2]Pick Off in the Power recycling cavity

Chapter 3

Length Sensing and Control Scheme

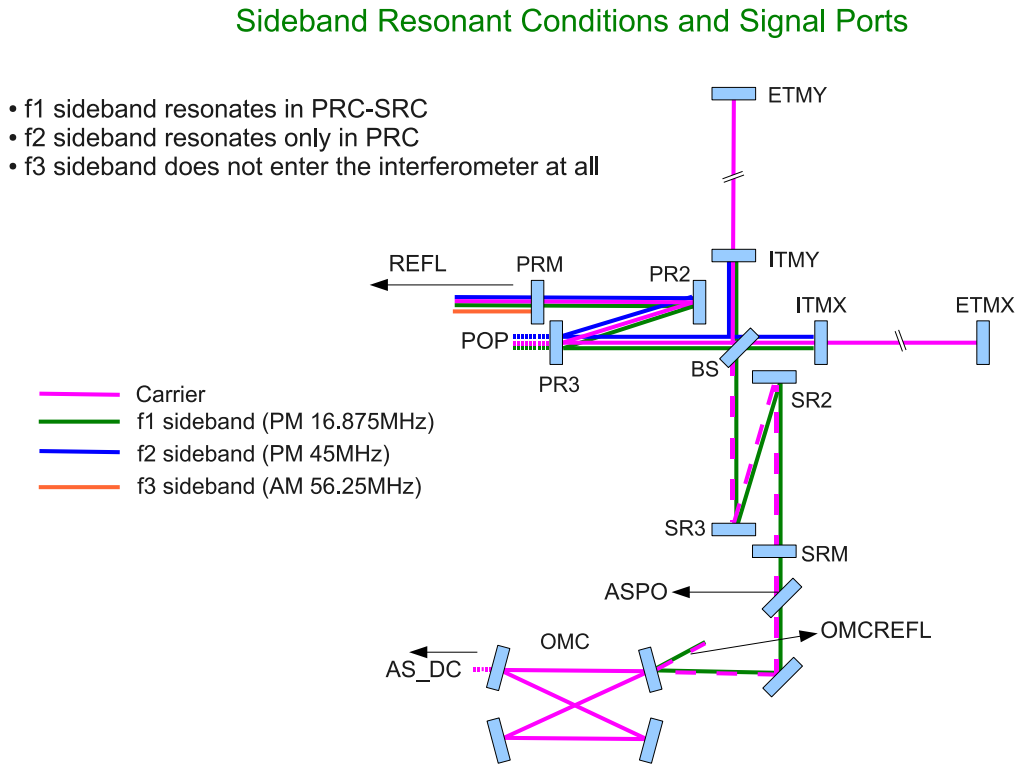

Figure 3.1: RF sideband resonant conditions and signal ports. POP is drawn at the transmission of PR3 to avoid congestion of the diagram. However, POP is actually planned to be picked up from the back of PR2 because the beam size is much smaller there.

f1	16.880962 MHz	$3 \times f_{\mathrm{MC}}$, PM
f2	45.015898 MHz	$8 \times f_{\mathrm{MC}}$, PM
f3	39.388910 MHz and 56.269873 MHz	$7 \times f_{\mathrm{MC}}$ and $10 \times f_{\mathrm{MC}}$, AM
f_{MC}	5.626987 MHz	MC FSR
L_{MC}	26.6388 m	MC Length

Table 3.1: RF Sideband Frequencies

3.1 Overview

The length degrees of freedom to be controlled are DARM, CARM, MICH, PRCL and SRCL (see appendix D for the definitions of the acronyms). These degrees of freedom are collectively called canonical degrees of freedom in this document. DARM is sensed at the AS port by the DC readout scheme. Other degrees of freedom are sensed by a variant of frontal modulation scheme. The input laser beam is phase or amplitude modulated to generate RF sidebands. There are two RF sidebands, which resonate in the central part (PRC, MICH, SRC) of the interferometer. The sideband resonant conditions are shown in Figure 3.1. The f1 sideband resonates in the compound cavity of PRC-SRC. The MICH reflectivity to the f2 sideband is chosen to be almost 100%. Consequently, f2 only resonates in PRC. Optionally, we may add another RF sideband, f3, which does not enter the interferometer at all. f3 is called a non-resonant sideband (NRS).

When operated in DRSE configuration, the detuning of the SRC is done by adding offset to the error signal of SRCL. The required detuning of SRC is 3.5 degree in terms of the one-way phase shift of SRCL, which corresponds to 10 nm shift of SRM position. The f1 sideband frequency is chosen to make the resonance of f1 to SRC not too sharp, so that the detuned SRC can still produce a reasonable error signal using f1. The SRCL error signal is plotted as a function of SRM position in Figure 2.16. The operating point of DRSE has enough slope to produce strong error signal. However, the non-linearity of the error signal is stronger at the DRSE operating point. Discussions on this non-linearity and other issues with the offset detuning of SRC can be found in Appendix B.

The selected RF modulation frequencies are listed in Table 3.1. The mode cleaner has to transmit the RF sidebands. For this reason, the FSR of the MC is chosen to be f2/8.

3.2 Simulation Conditions

The calculations shown in the following sections are all done by using a simulation tool called Optickle [8]. The interferometer model and simulation codes are available in the KAGRA svn at [9].

Arm Cavity Asymmetry

When perfoming simulations, we assumed the asymmetry of the arm cavity loss (round trip) to be ± 30 ppm, while the average loss is 100 ppm per round trip. This rather high asymmetry corresponds to about $\pm 1.5\%$ asymmetry of the finesse. As a consequence, the DC carrier power at the AS port without the differential arm cavity length offset is about 4 mW. We call this mis-match light or field, because it is produced by the loss mis-match between the two arm cavities.

The mis-match light itself is useless as a local oscillator for the DC readout, because it is orthogonal to the GW SBs. However, when combined with the DC field produced by the differential offset of the arm cavity lengths (we call it offset light), the homodyne angle can be set to be other than 90 dgrees. By properly chosing the homodyne agnle, we can perform the back action evasion (BAE) measurement, which can beat the standard quantum limit (SQL). The default homodyne angle of KAGRA for BRSE

is 58 degrees, which requires about 10 mW of the offset light, corresponding to ±2 pm of DARM offset. For BRSE, the homodyne angle is 45 degrees. The offset light is 4 mW corresponding to ±1.3 pm of DARM offset.

The amount of the loss asymmetry is not something we can precisely control. Therefore, the intensity of the mis-match light may be significantly larger or smaller than 4 mW. If the asymmetry is very large and the mis-match field is too strong, we consider it a failure of the mirror manufacturing. We have to avoid it by careful quality control of the mirror fabrication[1]. If the loss imbalance is too small, the required offset light power to realize the BAE becomes very small. This makes the requirements for the OMC very stringent, because the OMC has to reduce the RF SB and other junk fields well below the small local oscillator field. One solution to this problem is to increase the loss of one of the mirrors by, for example, slightly staining the surface. However, this is probably not a good idea and very difficult to do in a controlled manner. It is very likely that we damage the mirror. Thus not recommended. Another option is just to abandon the BAE. In this case, we lose 10 to 20 Mpc of the inspiral range[2].

PD

We all know that there is no good RF PD which can receive 1 W of light power. In the simulation, the DC light power falling on to any RF PD is limited to be equal to or smaller than 50 mW by, if necessary, inserting an attenuator, so that the shot noise estimates for the auxiliary DOFs are realistic.

3.3 Signal Name Convention

In this document, signal names follow the convention described here. A signal name consists of a port name followed by an indicator of demodulation scheme connected with an underscore (_). For example, "REFL_1I" means a signal detected at the reflection port and demodulated at the f1 frequency in I-phase. Another example is "AS_DC", which means a DC signal detected at the AS port.

Double demodulation may be used if we use the f3 sideband. In this case, a signal name looks like "REFL_1DmQ". This means a signal detected at the REFL port demodulated at f3-f1 frequency in Q-phase. Double demodulation is always between f3 and one of the other SBs. Therefore, only one number is specified. The letter "D" means double demodulation, "m" means f3 minus f1. In the case of f3 plus f1, this letter will be "p".

"REFL_1DmQ" is not a true double-demodulation, where the signal should be demodulated twice at f3 and f1 frequencies. However, it carries similar information as the true double-demodulation.

3.4 Signal Extraction Ports

The default length sensing scheme for bKAGRA uses two phase modulated RF sidebands, f1 and f2. The beat notes of these sidebands with the carrier are detected at the REFL and the POP ports to extract necessary error signals. The signal sensing matrices are shown in Table 3.2 and Table 3.3. The diagonal elements are the signals we plan to use as error signals. The shot noise of each signal is shown in Table 3.4 and Table 3.5. The shot noise matrices are calculated by first dividing the signal strength (in [W/m]) of each DOF at each signal port by the shot noise level (in $[\mathrm{W}/\sqrt{\mathrm{Hz}}]$) of the corresponding signal port, then inverting the result, to get the displacement equivalent noise in the unit of $[\mathrm{m}/\sqrt{\mathrm{Hz}}]$.

The CARM signal produces large non-diagonal elements to the PRCL and SRCL. This is because the phase change of the carrier by CARM is usually much larger than that of the RF sidebands by PRCL or SRCL. However, the CARM feedback loop can have a very large control gain because of the

[1] which is extreme difficult. We know it.
[2] Need to check the numbers.

	DARM	CARM	MICH	PRCL	SRCL
AS_DC	1.0	3.3×10^{-6}	7.2×10^{-4}	1.8×10^{-7}	5.0×10^{-5}
REFL_1I	9.6×10^{-3}	1.0	5.0×10^{-3}	6.2×10^{-2}	3.0×10^{-2}
REFL_1Q	7.1×10^{-3}	2.6×10^{-4}	1.0	8.5×10^{-2}	2.5×10^{-2}
POP_2I	5.4×10^{-2}	5.7	1.8×10^{-2}	1.0	2.7×10^{-4}
POP_1I	1.8×10^{-1}	19.0	1.1×10^{-1}	2.1	1.0

Table 3.2: Normalized Sensing Matrix of LSC in the case of BRSE. Each row is normalized by the diagonal element. The interferometer response was evaluated at 100 Hz to create this matrix.

	DARM	CARM	MICH	PRCL	SRCL
AS_DC	1.0	6.6×10^{-6}	7.1×10^{-4}	5.8×10^{-7}	5.8×10^{-5}
REFL_2I	1.4×10^{-2}	1.0	4.0×10^{-3}	4.3×10^{-2}	1.5×10^{-4}
REFL_1Q	2.5×10^{-1}	1.3	1.0	6.5×10^{-2}	3.4×10^{-2}
POP_2I	7.7×10^{-2}	5.7	1.8×10^{-2}	1.0	1.5×10^{-4}
POP_1I	4.7×10^{-1}	32.8	1.7×10^{-1}	2.0	1.0

Table 3.3: Normalized Sensing Matrix of LSC in the case of DRSE. Each row is normalized by the diagonal element. The interferometer response was evaluated at 100 Hz to create this matrix.

very fast nature of the laser frequency feedback. We can rely on this fact to suppress the interference of CARM to PRCL and SRCL (the gain hierarchy approach).

In REFL_1Q, the mixture of PRCL and SRCL to MICH is large. This does not happen when there is no asymmetry in the interferometer. The ±30 ppm loss asymmetry, as described in section 3.2, makes the CARM, PRCL and SRCL signals no longer be at exactly the orthogonal quadrature to the MICH signal. We chose a demodulation phase which minimizes the coupling of CARM. In return, the PRCL and SRCL signals became comparable to MICH. However, these signals cab be separated because the lower right 3×3 matrices of Table 3.2 and Table 3.3 are invertible.

If we use the f3 sideband, which is an AM non-resonant sideband, the sensing matrix looks like Table 3.6 (BRSE). Because the carrier is not involved in the signal generation of MICH, PRCL and SRCL, the large CARM interference disappeared in this case. So we don't have to rely on the gain hierarchy. However, in this configuration, we have to introduce a Mach-Zehnder interferometer at the modulation stage to separate the AM generation path and the PM generation path. This is necessary to avoid the generation of sub-sidebands at the double demodulation frequencies. The addition of Mach-

	DARM	CARM	MICH	PRCL	SRCL
AS_DC	6.7×10^{-21}	2.0×10^{-15}	9.3×10^{-18}	3.8×10^{-14}	1.3×10^{-16}
REFL_1I	1.0×10^{-16}	1.0×10^{-18}	2.0×10^{-16}	1.6×10^{-17}	3.3×10^{-17}
REFL_1Q	3.7×10^{-14}	1.0×10^{-12}	2.6×10^{-16}	3.1×10^{-15}	1.1×10^{-14}
POP_2I	2.8×10^{-15}	2.6×10^{-17}	8.5×10^{-15}	1.5×10^{-16}	5.5×10^{-13}
POP_1I	1.4×10^{-15}	1.3×10^{-17}	2.3×10^{-15}	1.2×10^{-16}	2.5×10^{-16}

Table 3.4: Shot noise matrix of LSC in the case of BRSE. The numbers represent the displacement equivalent shot noise [m/$\sqrt{\text{Hz}}$]. The interferometer response was evaluated at 100 Hz to create this matrix.

	DARM	CARM	MICH	PRCL	SRCL
AS_DC	4.6×10^{-21}	6.9×10^{-16}	6.4×10^{-18}	7.9×10^{-15}	7.9×10^{-17}
REFL_2I	4.3×10^{-16}	5.8×10^{-18}	1.4×10^{-15}	1.4×10^{-16}	3.8×10^{-14}
REFL_1Q	7.2×10^{-16}	1.3×10^{-16}	1.8×10^{-16}	2.8×10^{-15}	5.3×10^{-15}
POP_2I	1.9×10^{-15}	2.6×10^{-17}	8.5×10^{-15}	1.5×10^{-16}	1.0×10^{-12}
POP_1I	1.1×10^{-15}	1.6×10^{-17}	3.2×10^{-15}	2.6×10^{-16}	5.3×10^{-16}

Table 3.5: Shot noise matrix of LSC in the case of DRSE. The numbers represent the displacement equivalent shot noise [m/$\sqrt{\text{Hz}}$]. The interferometer response was evaluated at 100 Hz to create this matrix.

	DARM	CARM	MICH	PRCL	SRCL
AS_DC	1	4.1×10^{-5}	1.0×10^{-3}	4.8×10^{-6}	4.7×10^{-6}
REFL_1I	5.4×10^{-3}	1	3.9×10^{-5}	5.4×10^{-3}	4.5×10^{-3}
REFL_1DmQ	4.8×10^{-3}	2.5×10^{-3}	1	0.7	1.3×10^{-3}
REFL_2DmI	1.83×10^{-3}	8.3×10^{-2}	0.18	1	0.32
REFL_1DmI	2.5×10^{-4}	1.5×10^{-2}	2.4×10^{-2}	1.7	1

Table 3.6: Normalized Sensing Matrix of LSC for BRSE using the f3 sideband. Each row is normalized by the diagonal element. The interferometer response was evaluated at 100 Hz to create this matrix.

Zehnder may introduce additional noise. Moreover, the generation of AM sidebands is not as easy as one might think. A simple AM generator wastes a lot of laser power [10]. A clever idea is proposed to avoid this problem [10]. However, it is still at a proof-of-concept stage.

There is another potential problem with the f3 scheme. In this schem, the carrier does not contribute to the the signal generation of the central part. Therefore, it just increase the shot noise if present at detection ports. At REFL, the amount of the carrier power returning from the interferometer depends on the reflectivity matching of the PRM and the Fabry-Perot Michelson part. The reflectivity of the FPMI depends heavily on the loss of the arm cavities, hence very difficult to precisely control. If the matching is poor, a lot of carrier power will come back to the REFL port. This has a potential of increasing the shot noise of the signals detected at REFL by a large factor.

For the above mentioned reasons, we do not employ the f3 scheme during the observation mode of KAGRA. However, we can still use this scheme during the lock acquisition, where the noise is not so important but the stability and robustness of the error signals is critical.

3.5 Loop Noise

3.5.1 Servo loop model

In general, the auxiliary degrees of freedom have larger shot noise than DARM. By using those signals for mirror control, we are effectively injecting extra noise into the interferometer. Especially, MICH has an unavoidable coupling to DARM by about 1/Finesse. Therefore, the shot noise of the MICH error signal appears to DARM attenuated by this factor. This noise coupling mechanism is called loop noise and one needs to pay close attention to this when designing an interferometer control scheme.

Figure 3.2 shows a block diagram of the servo loops for the interferometer control. The detector matrix D converts the real DOF vector $\vec{x}$, which represents the mirror displacements and other dynamic elements in the interferometer, such as laser frequency, into a vector of error signals $\vec{\epsilon}$ in the canonical

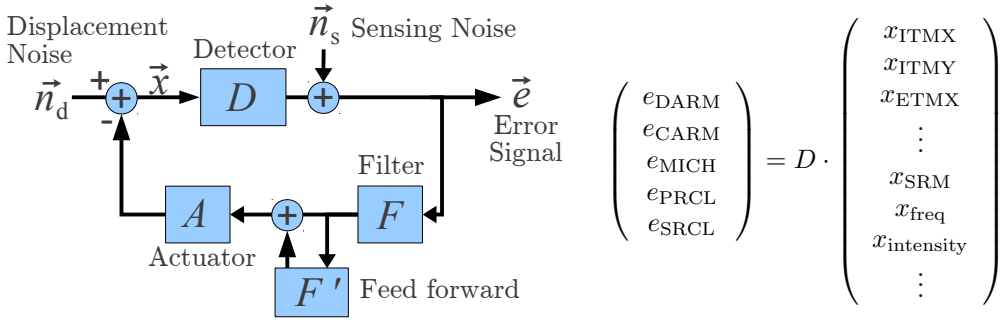

Figure 3.2: Block diagram of the feedback loops. The real DOF vector $\vec{x}$ contains the displacement of each mirror and other dynamic degrees of freedom in the interferometer, such as laser frequency and intensity. It is converted to the vector $\vec{e}$ of the error signals in the canonical DOFs by the detector matrix D. All the matrices in the figure are frequency dependent.

DOFs. Then the sensing noise vector, $\vec{n_{\rm s}}$, is added to the error signal vector. $\vec{n_{\rm s}}$ represents shot noise and any other noise added at the sensing stage, such as PD noise.

D and $\vec{n_{\rm s}}$ are calculated by Optickle. The error signals are filtered by a feedback filter F and fed back to the mirrors through the actuator matrix A, which converts feedback signals in the canonical DOFs to the real DOFs of the interferometer. Then the disturbance vector $\vec{n_{\rm d}}$ is added before the sensing matrix D. $\vec{n_{\rm d}}$ represents disturbances to the interferometer, such as the mirror displacement noises and the laser frequency noise.

The DARM error signal is the first element of the error signal vector $\vec{e}$. In the absence of gravitational waves, $\vec{e}$ is written as,

$$\vec{e} = (I+G)^{-1} \cdot \vec{n_{\rm s}} + (I+G)^{-1} \cdot D \cdot \vec{n_{\rm d}}, \tag{3.1}$$

$$G \equiv D \cdot A \cdot (I+F') \cdot F, \tag{3.2}$$

where I is the identity matrix. The off-diagonal elements of $(I+G)^{-1}$ are responsible for the loop noise couplings.

The shot noise coupling by the control loops was calculated using the above formla. We assumed the unity gain frequencies of the servo loops shown in Table 3.7.

	BRSE	**DRSE**
DARM	200 Hz	200 Hz
CARM	10 kHz	10 kHz
MICH	50 Hz	50 Hz
PRCL	50 Hz	50 Hz
SRCL	50 Hz	50 Hz

Table 3.7: Control Loop UGFs

The loop noise contributions from the auxiliary degrees of freedom are shown for the BRSE case in Figure 3.3 and Figure 3.4. The curves labeled Target are the target sensitivity. It is clear that loop noise couplings from other degrees of freedom are larger than the target level.

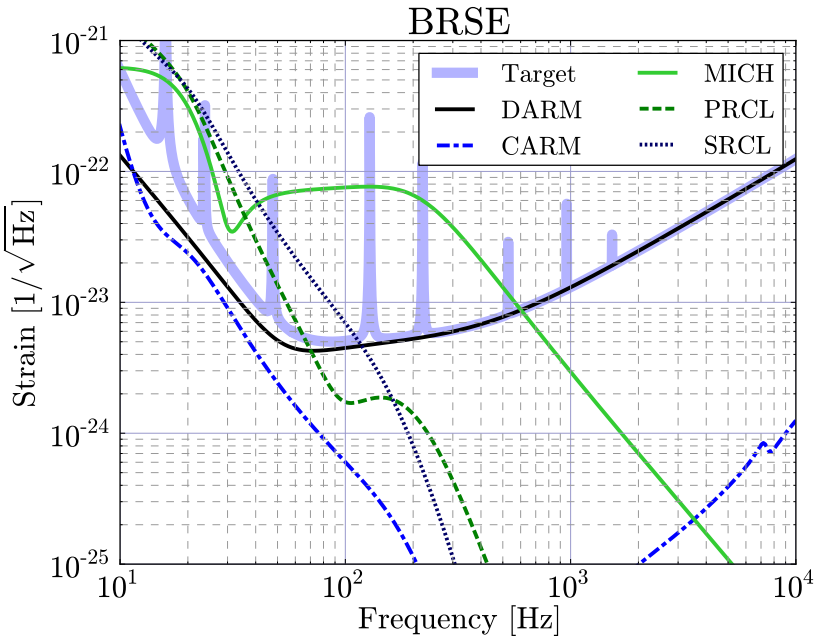

Figure 3.3: Loop Noise Coupling: BRSE

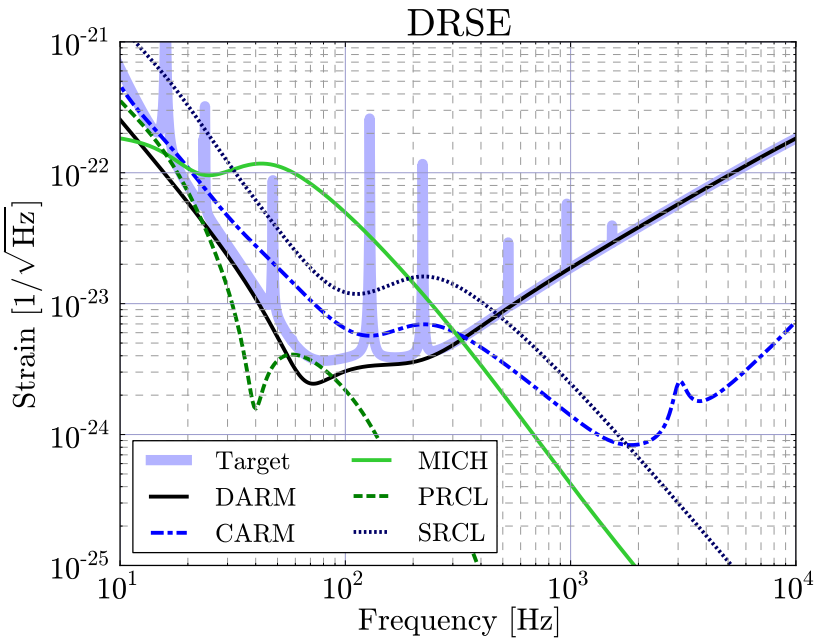

Figure 3.4: Loop Noise Coupling: DRSE

3.5.2 Feed forward

The loop noise coupling can be reduced by a technique called feed forward [11]. Its working principle is the following. Taking MICH as an example, we can measure the transfer function from the motion of BS[3] to the DARM signal. Then we assume that the error signal of MICH is dominated by the shot noise (or any sensing noise). This means that BS is moved by the shot noise through the feedback. From the feedback signal, we know exactly how much the BS is erroneously moved. Therefore, we can predict how much noise is injected from this BS motion to DARM with the knowledge of the above mentioned transfer function. By feeding forward this information to DARM, we can subtract the loop injected noise. The feed forward path is indicated in Figure 3.2 by F'.

The performance of feed forward is measured by the accuracy of the subtraction. Feed forward gain is defined as the inverse of the accuracy. If the accuracy is 1%, the feed forward gain is 100, which means that the loop noise couplings can be reduced by a factor of 100.

In Figure 3.5and Figure 3.6, the loop noise couplings are shown when the feed forward is applied with the gain of 100 to MICH, PRCL and SRC. With the feed forward, the loop noise couplings can be reduced well below the DARM quantum noise.

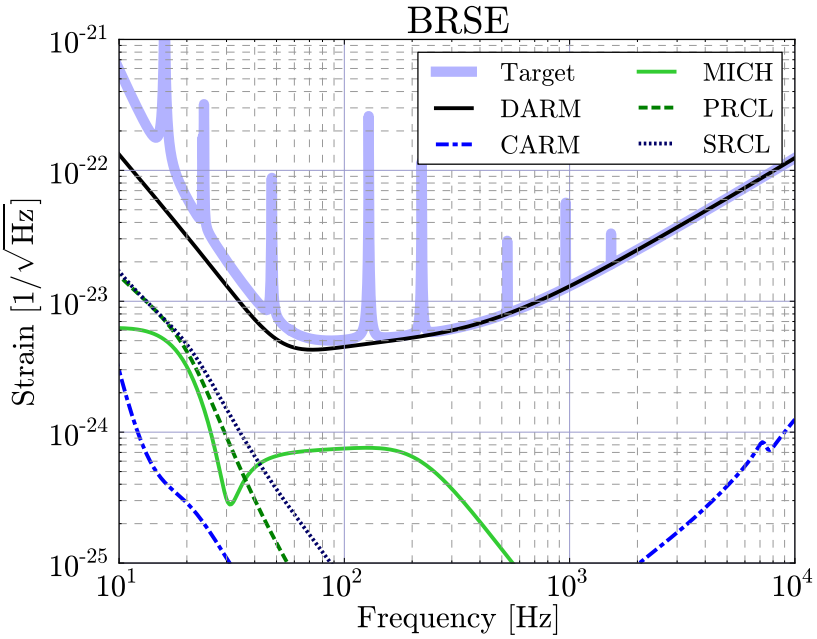

Figure 3.5: Loop Noise Coupling with Feed Forward: BRSE

3.6 PD Dynamic Range

The intrinsic noises of photo detectors is another important class of sensing noise. A PD always receives some offset light, either in RF or DC depending on the type of PD. At some ports, these offset signals can be very large. In this case, the dynamic ranges of the PD becomes an issue.

[3]The feedback point for MICH. Actually, we also move PRM and SRM by $1/\sqrt{2}$ to compensate for the changes in PRCL and SRCL.

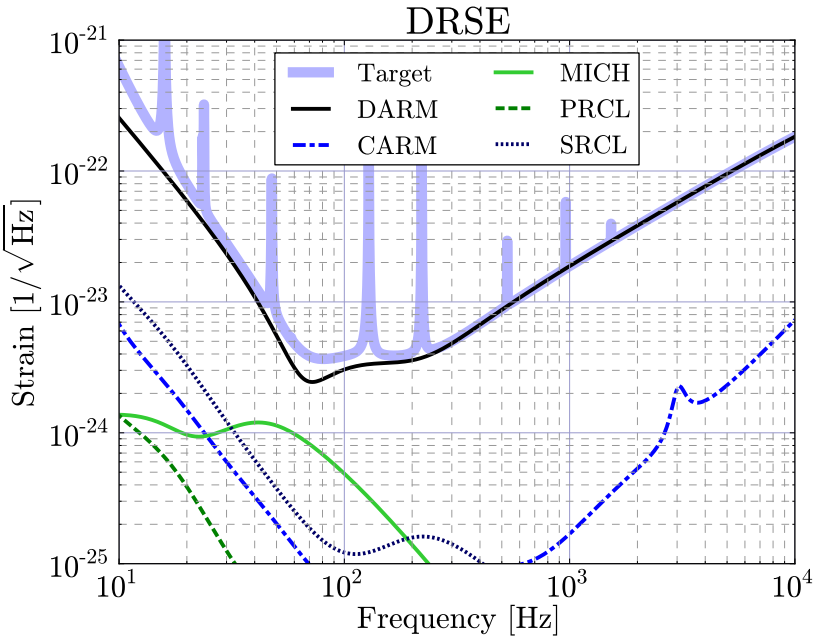

Figure 3.6: Loop Noise Coupling with Feed Forward: DRSE

Typically, a low-noise fast operational amplifier (op-amp) used for the current to voltage conversion of a PD has a dynamic range of about 200 dB according to the catalog specifications [12]. However, because of the slew rate limit, the actual dynamic range at RF is much smaller. Moreover, in order to minimize the non-linearity of the detector response, we want to use the op-amps at a much smaller signal level than the slew rate limit. Therefore, for the following analysis, we assume the dynamic range to be 160 dB for RF PDs and 190 dB for a DC PD.

Once the dynamic range D is specified, the sensing noise, n_{pd}, of a PD, in terms of the equivalent signal light power on the PD, can be expressed as $n_{\mathrm{pd}} = P_{\mathrm{ofs}}/D$, where P_{ofs} is the offset signal power for the PD. Then we can simply replace n_{s} in (3.1) with n_{pd} to calculate the loop noise couplings for the PD noise.

Figure 3.8 and Figure 3.8 show the calculated PD noise couplings for BRSE and DRSE. The PD noises are large in the DRSE mode, especially for MICH. It is because the SRC detuning changes the relative phase of the f1 sidebands with the carrier so that they no longer form a pure phase modulation. The result is constant large RF signals on the PDs for the signals using the f1 sidebands. Since the PD noise is a kind of sensing noise, with the use of feed forward, it can be reduced. Figure 3.9 and Figure 3.10 show the PD noise contributions after the feed forward is applied. Even for the DRSE case, the noises are below the target sensitivity.

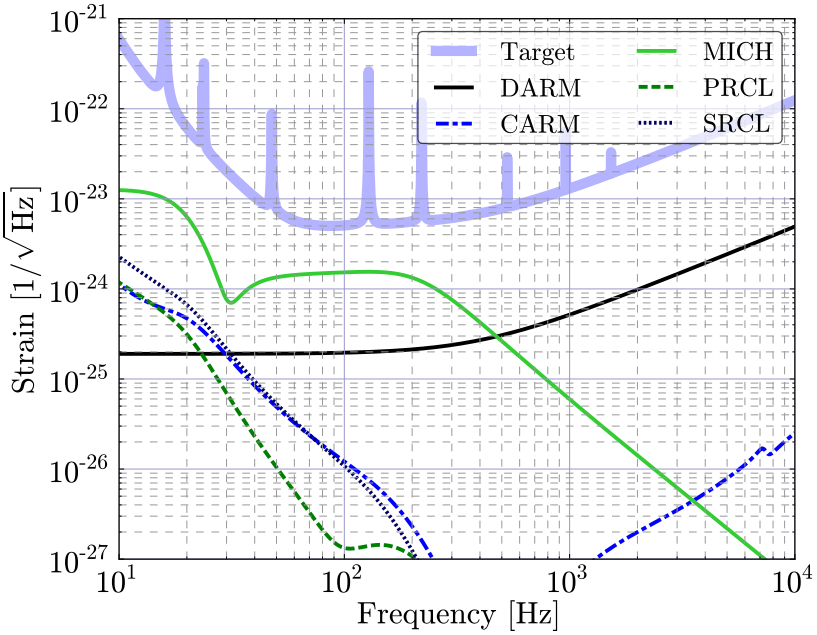

Figure 3.7: PD noise coupling: BRSE.

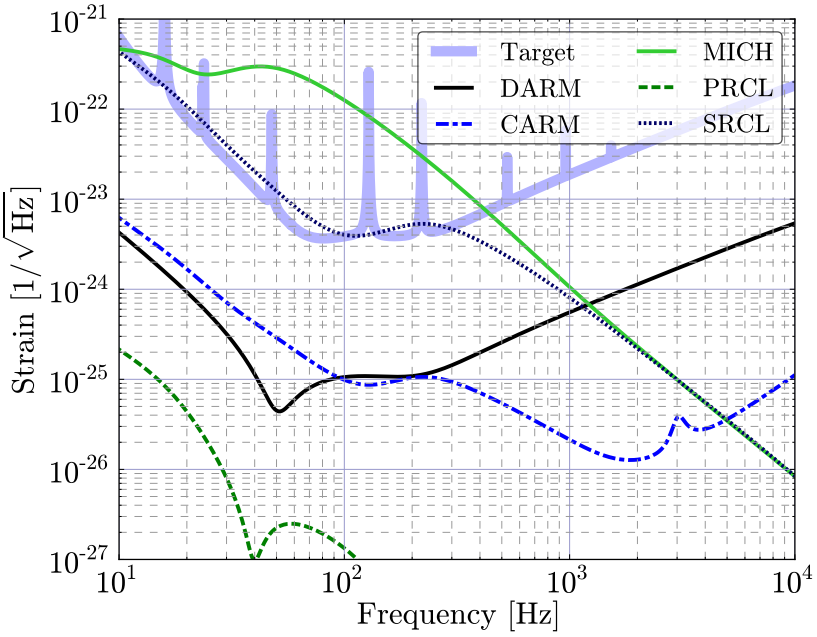

Figure 3.8: PD noise coupling: DRSE.

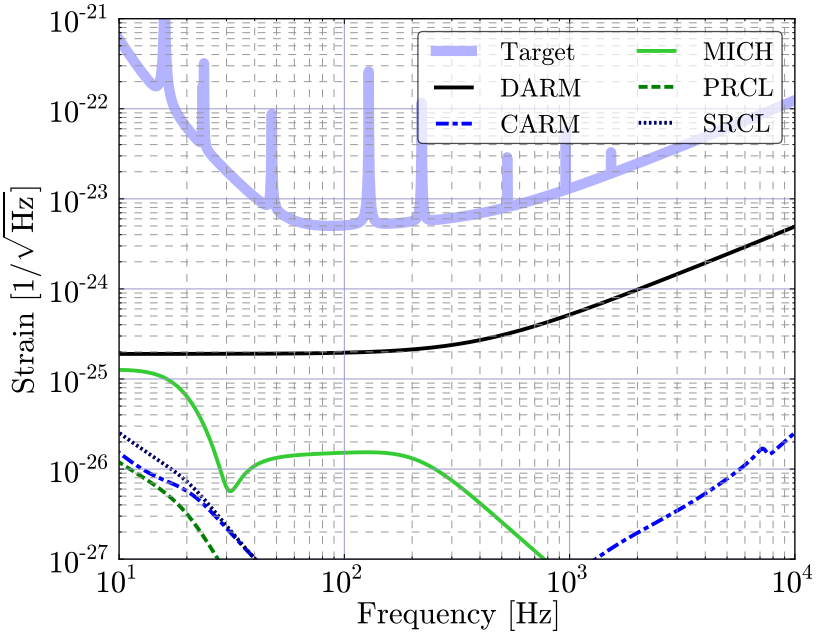

Figure 3.9: PD noise coupling with feed forward: BRSE.

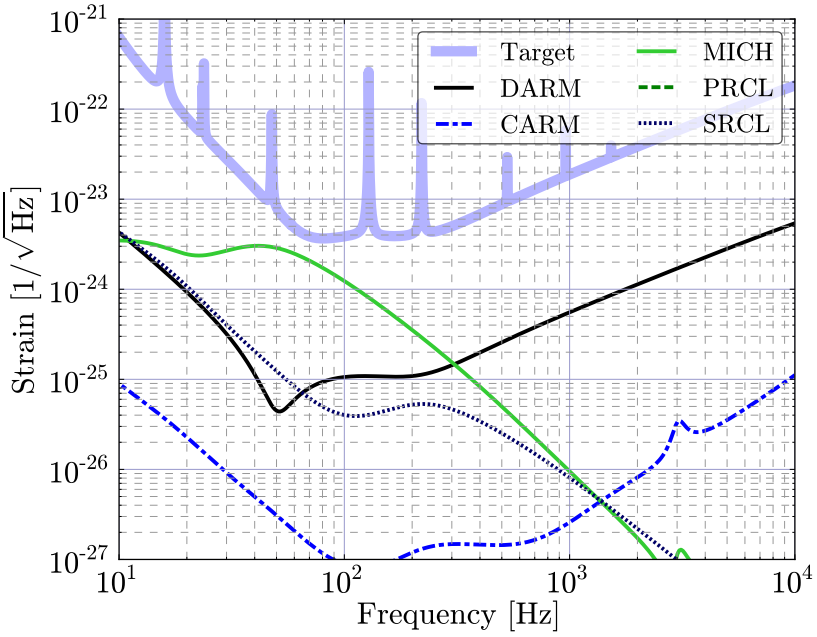

Figure 3.10: PD noise coupling with feed forward: DRSE.

Chapter 4

Noise Requirements

In this chapter, contributions of various noise sources, such as mirror displacement noise and laser noises, to the DARM error signal are calculated to set the requirements to those noises. The formalism of the calculation is basically the same for all the noise sources: Solving the equation (3.1) for $\vec{n_{\mathrm{d}}}$ and plugging in the target sensitivity into the first element of $\vec{e}$, which is the DARM error signal, we get the critical noise levels for all the disturbances in $\vec{n_{\mathrm{d}}}$. The critical noise level is defined as the amount of noise which produces the same noise level as the target sensitivity at the DARM. Since there are many noise sources, we require that contribution of each noise is 10 times smaller than the target sensitivity. Assuming all the noises are uncorrelated, we can allow 100 different kinds of noise sources to present before compromising the target sensitivity. Please note that *all the noise requirements below include the safety factor of 10.*

4.1 Mirror Displacement Noise

One caveat of feed forward is that it can increase the displacement noise coupling of the auxiliary degrees of freedom to DARM. Feed forward assumes that whatever you see in the error signal of an auxiliary degree of freedom, say PRC, is sensing noise, i.e. not a real motion of the mirror. This assumption is not valid in some frequencies. If the error signal reflects real motion of the mirror, this motion is suppressed by the feedback. Feeding forward this error signal to DARM means that you are trying to cancel the motion of the mirror (PRM) which is already suppressed by the (PRCL) feedback. The net result of this is the injection of the displacement noise of the auxiliary degrees of freedom into DARM.

One can calculate the transfer functions from the motion of auxiliary degrees of freedom to DARM with the feedback and the feed forward engaged. By requiring the displacement noise couplings to be a factor of 10 below the quantum noise of DARM, we can deduce the requirements to the displacement noise for each degree of freedom. The calculated displacement noise requirements are shown in Figure 4.1 (BRSE) and Figure 4.2. The current estimates of the auxiliary suspension (Type-B SAS) seismic noises are plotted alongside. Except for at several mechanical renonances, the displacement noise requirements are met.

4.2 Laser Noises

Contributions of the laser noises (frequency and intensity) are estimated by adding phase and amplitude modulators before the PRM in the Optickle model. The frequency noise requirement is calculated from the phase noise requirement by multiplying it with $2\pi f$, where f is the frequency of interest. The

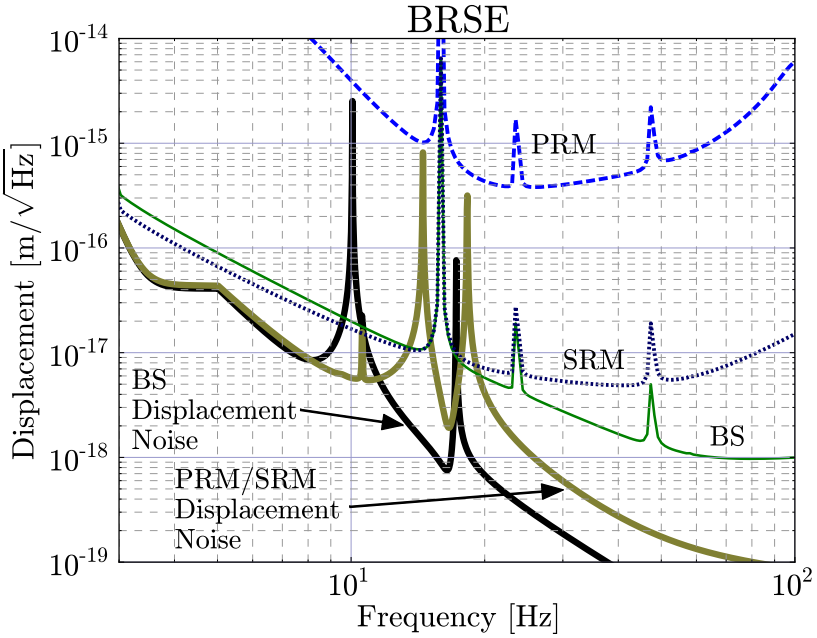

Figure 4.1: Displacement noise requirements for auxiliary mirrors: BRSE

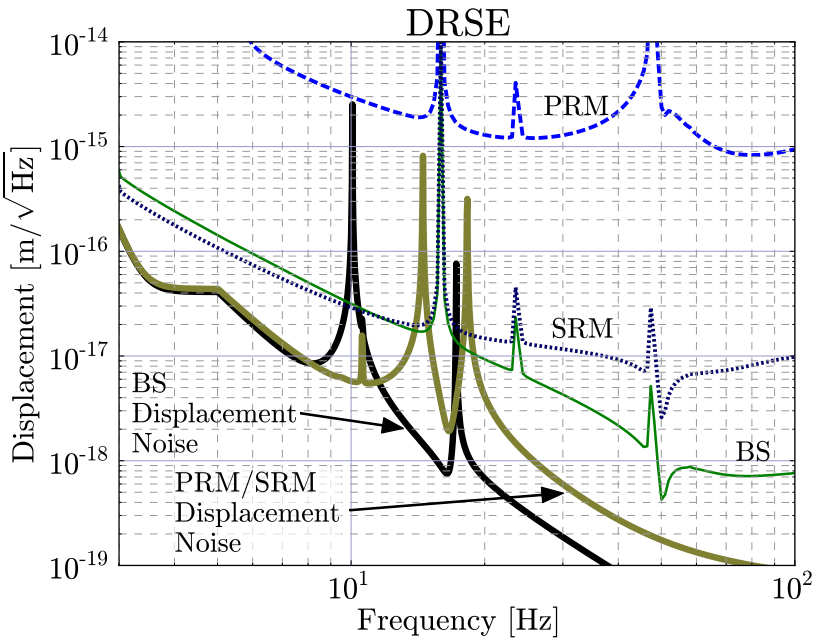

Figure 4.2: Displacement noise requirements for auxiliary mirrors: DRSE

amplitude noise can be converted to the relative intensity noise (RIN) just by multiplying with 2[1].

4.2.1 Frequency stabilization servo

The frequency noise stabilization servo will be a complex multiple loop system. A conceptual diagram of the frequency stabilization system (FSS) is shown in Figure 4.3.

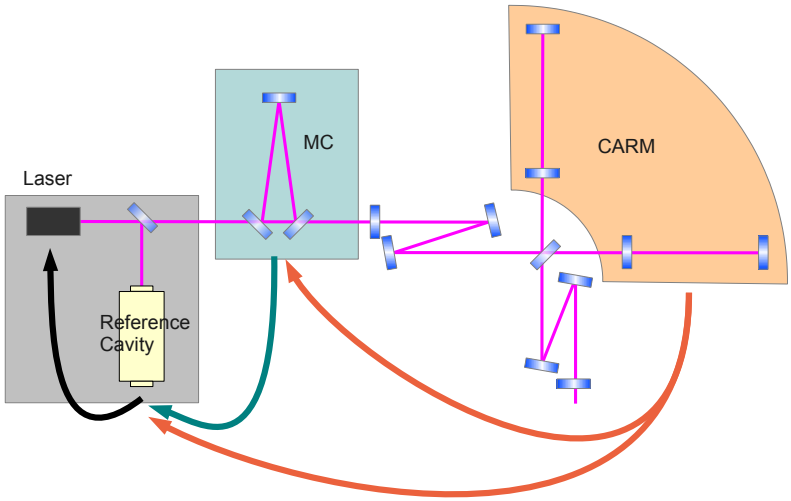

Figure 4.3: Conceptual diagram of the frequency stabilization system

At the beginning, the laser is locked to a rigid cavity called pre mode cleaner (PMC). The PMC serves as the absolute reference at low frequencies, typically below a few Hz. Then the laser is locked to a suspended MC. The error signal of the MC is fed back to the MC mirrors at low frequencies, where the mirror displacement noise is large, and to the error point of the PMC at high frequencies. Therefore, at high frequencies the laser frequency is locked to the MC length. Finally, the CARM used as the absolute reference of laser frequency in the observation frequency band. The CARM error signal is, again, fed back to the ETMs at low frequencies, and to the MC end mirror in the middle frequency range. At very high frequencies (above 50kHz or so), the error signal will be added to the MC error point, which is directly passed to the PMC error point.

Details of the FSS servo topology is yet to be designed. Therefore, in the next section, we treat whole the input laser system, from the laser source to the output of the MC, as a black box. Then we assume that the CARM error signal is fed back to the frequency actuator of this black box. The feedback UGF is assumed to be 10 kHz. The frequency noise requirement calculated with this model is equivalent to the frequency noise requirement to the MC output.

4.2.2 Frequency noise requirement

The frequency noise requirements with the safety factor of 10 are shown in Figure 4.4 and Figure 4.5. As mentioned above, these are the frequency noise requirements to the MC output. The frequency noise of the MC output is ultimately determined by the displacement noise of the MC mirrors (seismic and thermal). Therefore, it is interesting to convert the frequency noise requirements to the displacement

[1] $dP/P = 2 \cdot dE/E$

noise requirements. Figure 4.6 and Figure 4.7 show these requirements alongside the estimated MC susension seismic noise.

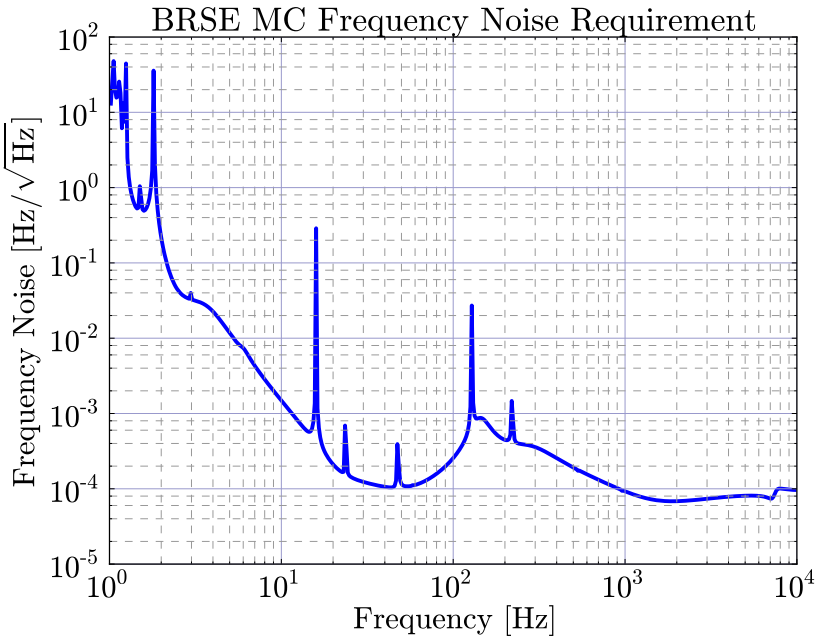

Figure 4.4: Laser frequency noise requirement at the output of the MC: BRSE

4.2.3 Intensity noise

The requirements on the relative intensity noise (RIN) of the laser are shown in Figure 4.8 and Figure 4.9. Since the Optickle can simulate the radiation pressure properly, the calculated results include the noise generation by the radiation pressure induced mirror motion.

4.3 RF Oscillator Noises

Phase and amplitude noises of the RF oscillators driving the phase modulators to generate the RF SBs produce noises in the error signals of the auxiliary DOFs, which use the RF SBs for error signal extraction. The feedback of those noises into the mirrors inject noises into DARM error signal, even though it uses DC readout.

4.3.1 Phase Noise

It is a common practice to express the phase noise of an oscillator in terms of the single sideband (SSB) phase noise. It is the power ratio of the carrier and the sideband which is generated by the phase noise at a particular frequency offset from the carrier frequency. The unit is dBc. Figure 4.10 and Figure 4.11 show the phase noise requirements of the RF oscillators in terms of SSB phase noise.

Good commercially available oven controlled crystal oscillators (OCXOs) have SSB phase noise of better than -150dBc. However, the requirement of DRSE (about -180dBc at a few tens of Hz) is

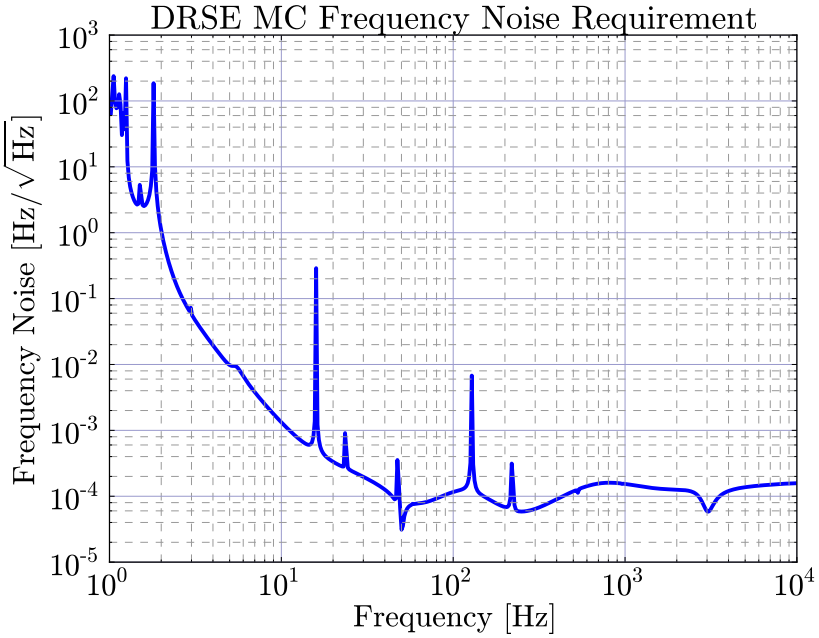

Figure 4.5: Laser frequency noise requirement at the output of the MC: DRSE

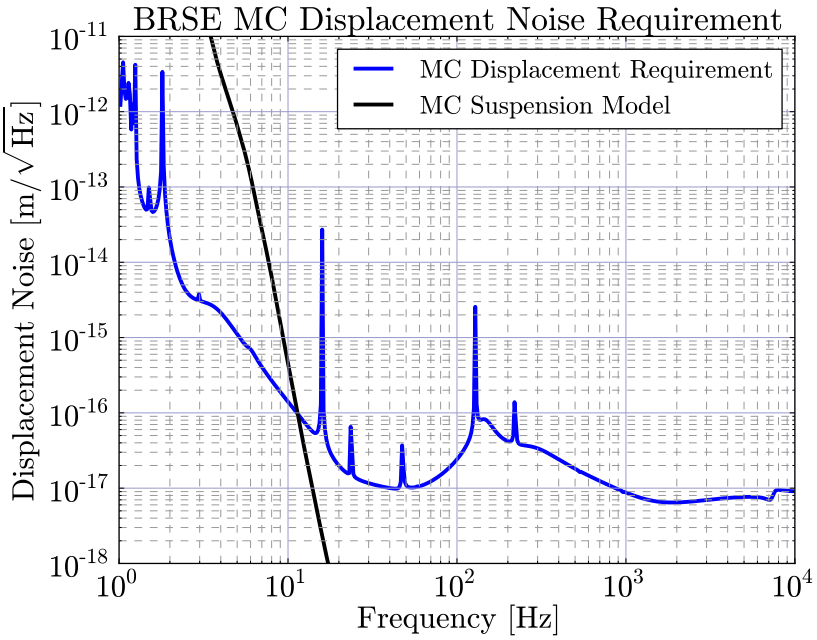

Figure 4.6: Displacement noise requirement for the MC suspension: BRSE

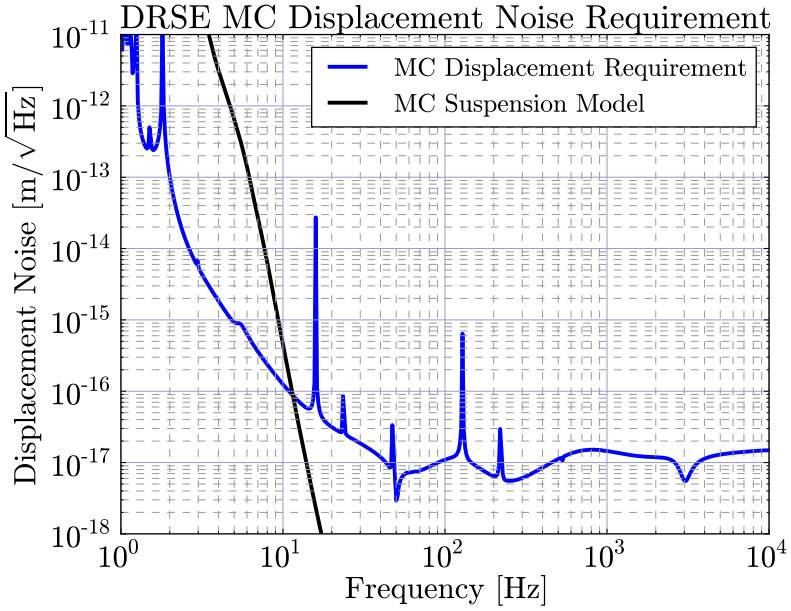

Figure 4.7: Displacement noise requirement for the MC suspension: DRSE

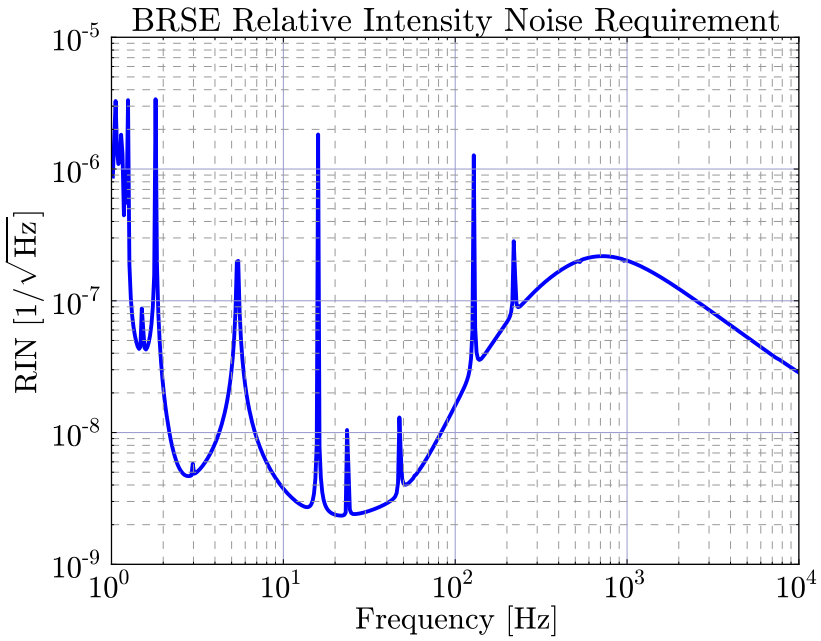

Figure 4.8: Relative Intensity Noise (RIN) requirement: BRSE

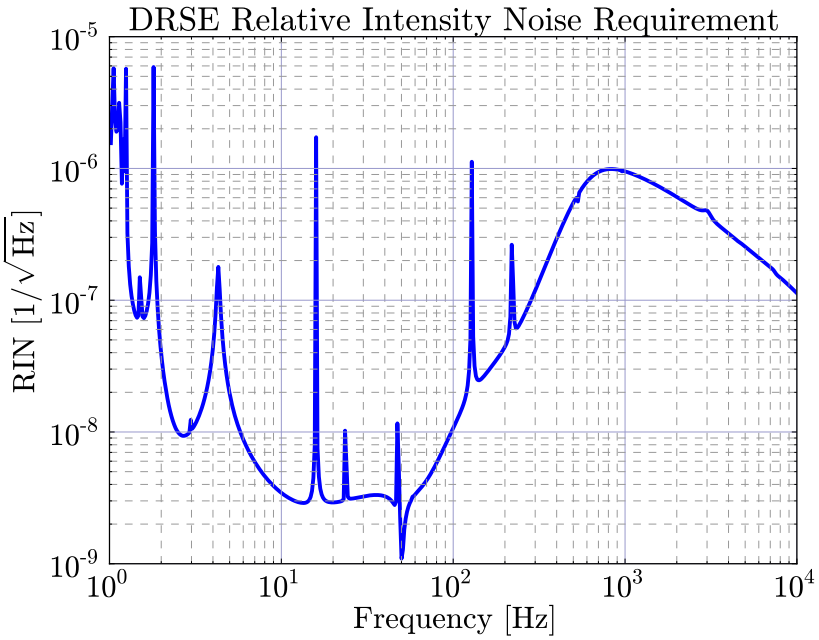

Figure 4.9: Relative Intensity Noise (RIN) requirement: DRSE

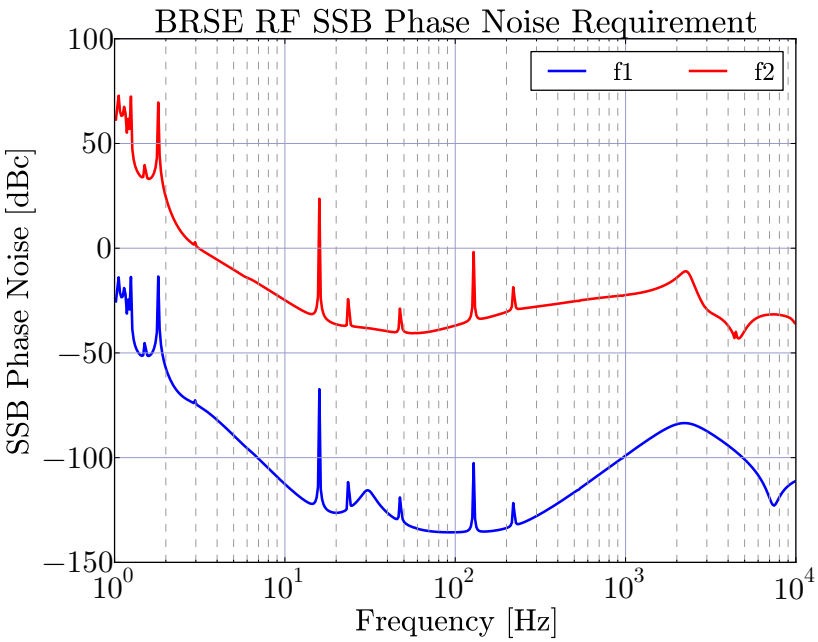

Figure 4.10: SSB Phase noise requirements: BRSE

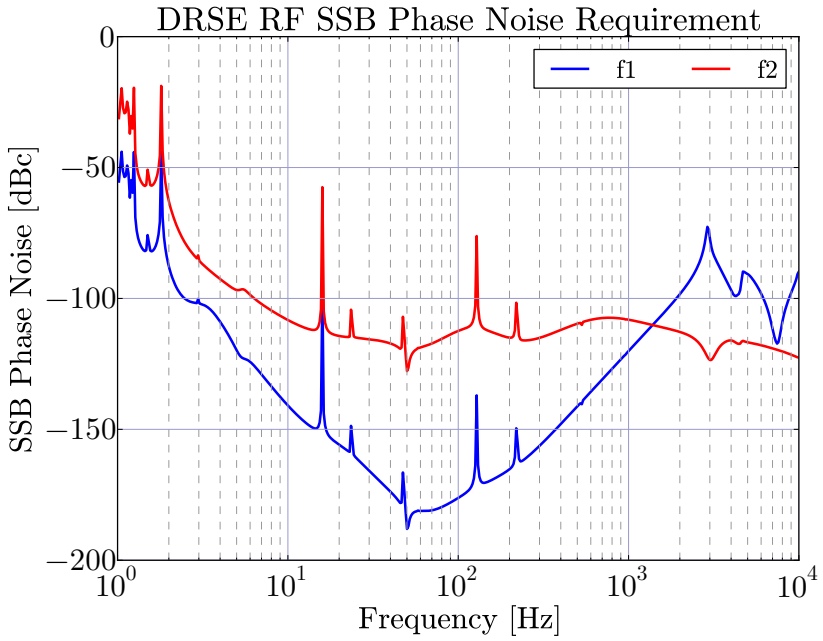

Figure 4.11: SSB Phase noise requirements: DRSE

extremely difficult to meet. One reason for the requirement being so stringent for DRSE is that, as explained in section 3.6, the SRC detuning causes the conversion of the purely phase modulated f1 SB into a mixture of amplitude and phase modulations. This AM creates offset in the error signals using the f1 SB. Then the oscillator phase noise directly changes the amount of the offset. A possible solution to this problem is to prepare the f1 SB as a mixture of PM and AM in the beginning. This idea is discussed in appendix C.

4.3.2 Amplitude Noise

The requirements on the relative amplitude noise of the RF oscillators are shown in Figure 4.12 and Figure 4.13. Please note that these are *amplitude* noise, not *intensity*.

4.4 Scattered Light Noise

A generic model of scattered light noise can be constructed as follows: A stray beam from the interferometer hits something, like a wall of a vacuum chamber. The surface of this object is vibrating so that the reflected light from the surface gets some phase fluctuations. A small fraction of the light reflected or scattered by this surface comes back to the interferometer. This scattered light field returning to the interferometer is denoted by E_{SCL}. Assuming the power spectrum density of the surface vibration is $A(\omega)[\mathrm{m}/\sqrt{\mathrm{Hz}}]$, the phase fluctuation of E_{SCL} is $2kA(\omega)$, where k is the wavenumber of light. Once entered into the interferometer, E_{SCL} propagates through the interferometer and interferes with the other fields to create noises in the error signals.

The contributions of scattered light to the interferometer outputs are calculated with the Optickle model by adding injection ports for scattered light at several locations. For example, in order to

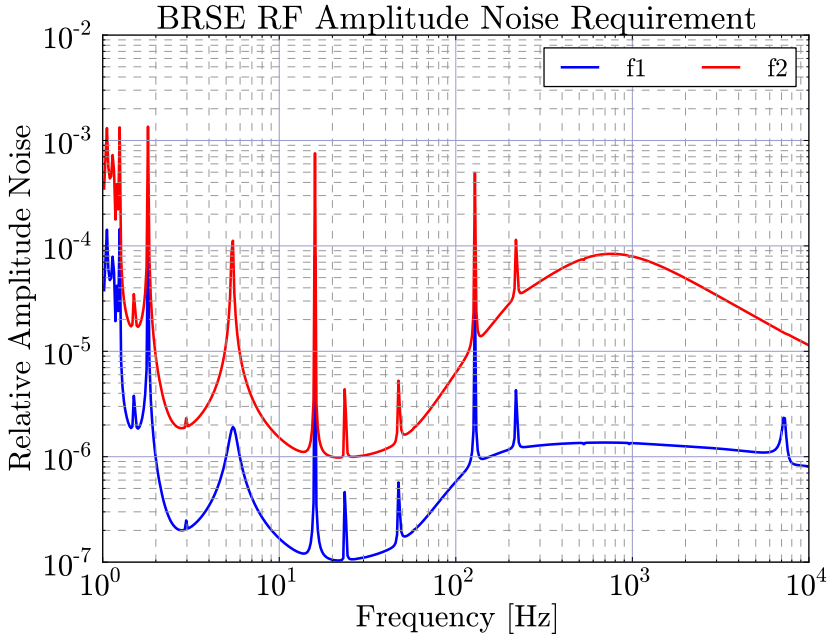

Figure 4.12: RF oscillator amplitude noise requirements: BRSE

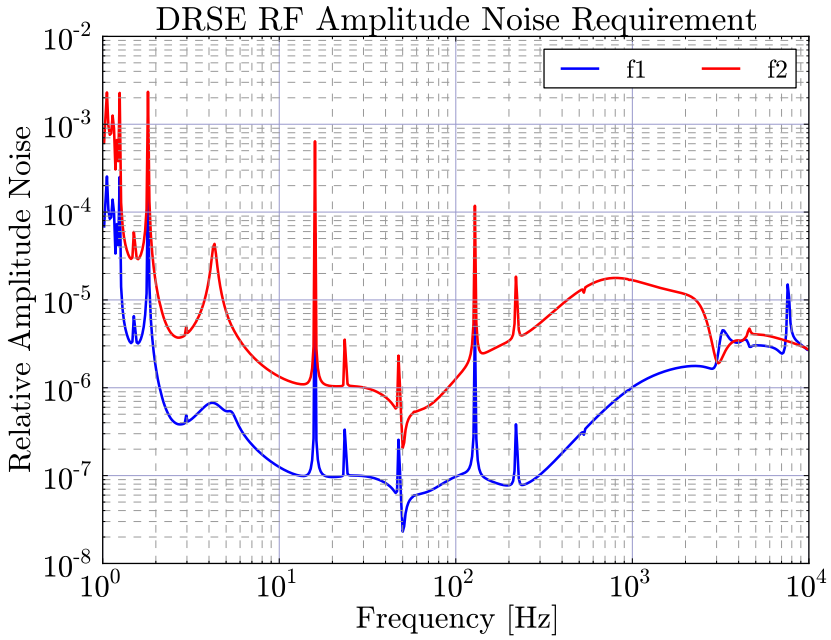

Figure 4.13: RF oscillator amplitude noise requirements: DRSE

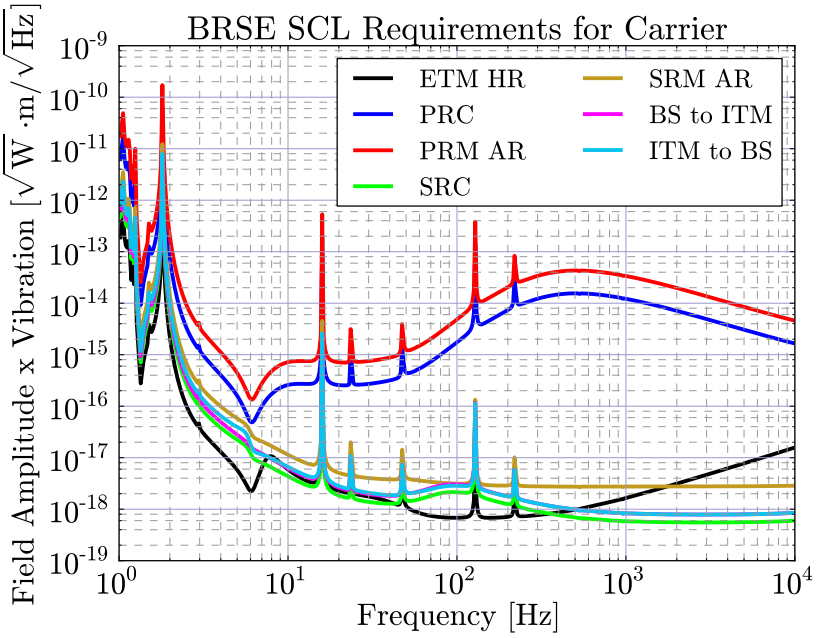

Figure 4.14: Scattered light requirements for the carrier: BRSE

simulate scattered light injection to the back of PRM, a low reflectivity pick-off mirror of 50 ppm is inserted just before the main beam from the MC hits the back of the PRM. Then a light source for simulating a scattered light field is added to the model. The beam from this source is passed through a phase modulator and injected to the interferometer through the pick-off mirror. The transfer functions from this phase modulator to various signal ports of the interferometer are calculated to estimate the magnitudes of scattered light noise couplings.

The relative phase between the additional light source and the carrier field is important. In the real interferometer, this is a random number. In the simulation, we injected the simulated scattered light in two orthogonal phases relative to the carrier. Then we took the squared sum of the transfer functions from the two injection phases to estimate the worst noise coupling.

The phase modulator explained above is a kind of disturbance to the interferometer. So it can be included as an element of $\vec{n_{\mathrm{d}}}$. Then the requirments on this disturbance can be calculated as described in 4. Since our model includes the feedback and feed forward loops, the scattered light noise couplings through the control loops of the auxiliary DOFs are automatically included in the results.

The scattered light can be at the carrier frequency or one of the RF SB frequencies. So we repeated the simulation changing the frequency of the scattered light source. If the scattered light field with an RF SB frequency enters the interferometer, it will not directly interfere with the GW SBs at the AS port. Rather, it will disturb the error signals for the auxiliary DOFs. Through the feed back loops, the scattered light induced disturbances appear in the DARM signal.

Figure 4.14 and Figure 4.17 show the requirements on the scattered light fields at the carrier frequency entering from various parts of the interferometer. The meaning of the curves is the following: The product of the field amplitude $E_{\mathrm{SCL}}[\sqrt{\mathrm{W}}]$ and the vibration amplitude $A(\omega)[\mathrm{m}/\sqrt{\mathrm{Hz}}]$ must be smaller than the curves. Similar requirements can be calculated for scattered light fields with RF SB frequencies and shown in Figure 4.15 to 4.19.

Figure 4.20 to Figure 4.25 show the coupling coefficients of the scattered light noise from various

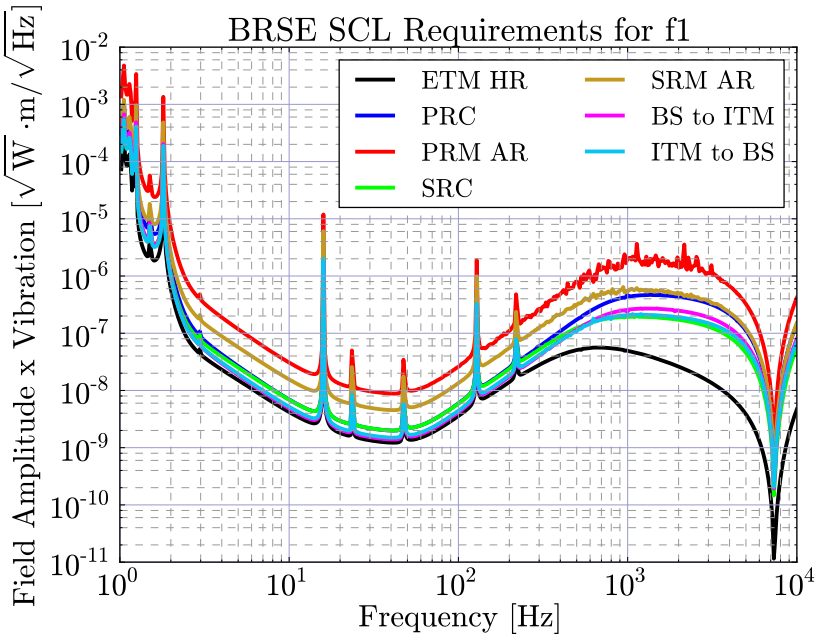

Figure 4.15: Scattered light requirements for the f1 RFSB: BRSE

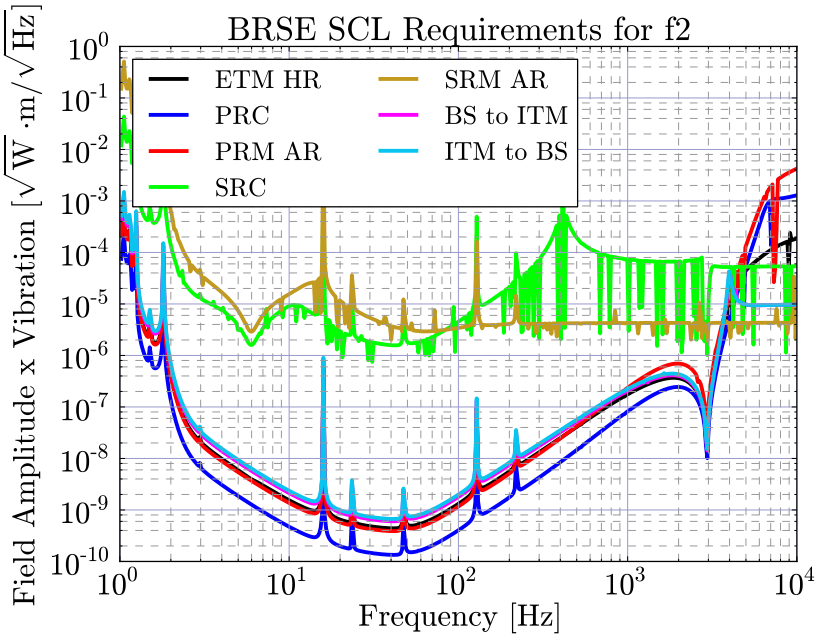

Figure 4.16: Scattered light requirements for the f2 RFSB: BRSE

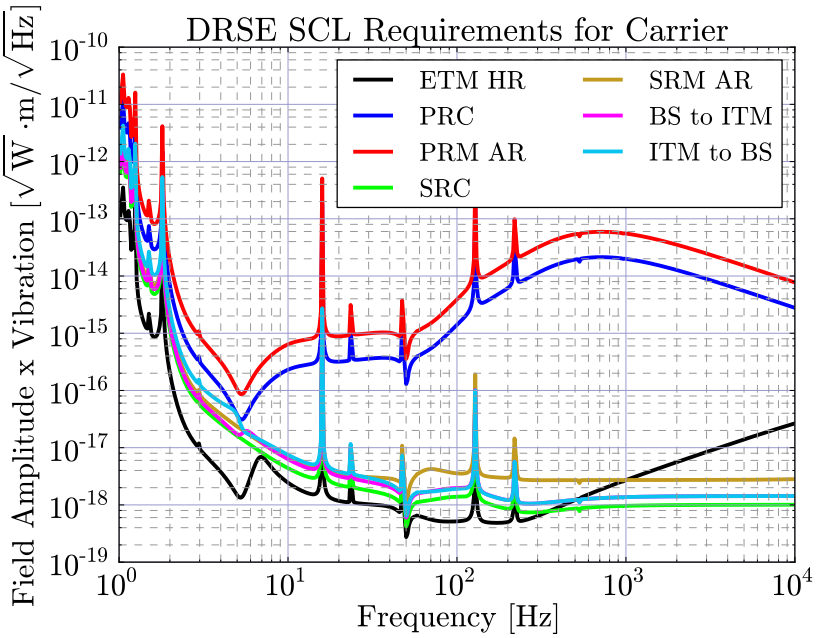

Figure 4.17: Scattered light requirements for the carrier: DRSE

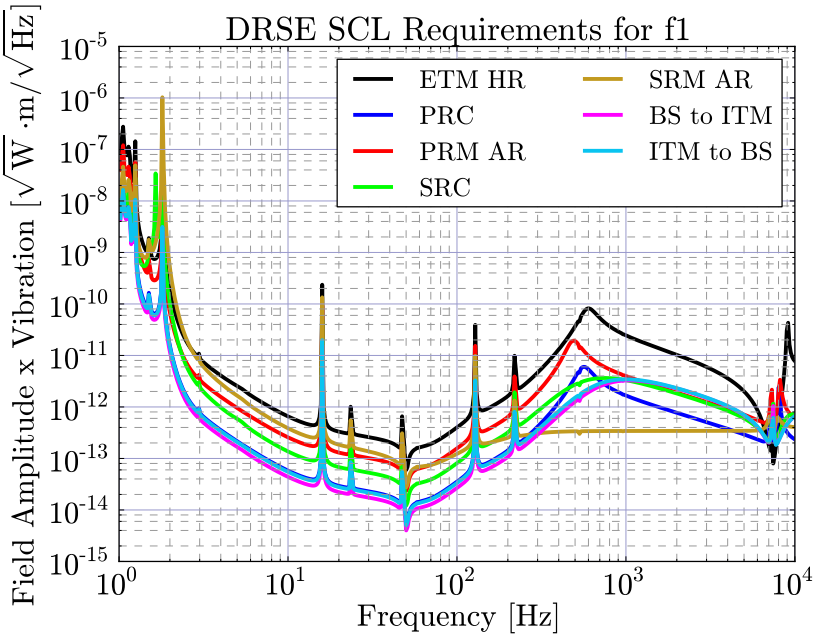

Figure 4.18: Scattered light requirements for the f1 RFSB: DRSE

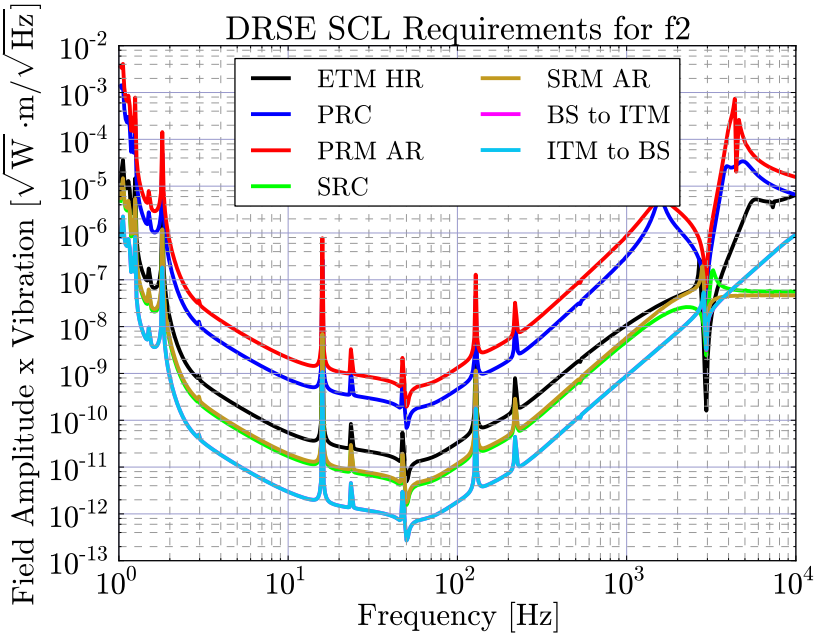

Figure 4.19: Scattered light requirements for the f2 RFSB: DRSE

Arm cavity (carrier)	250 kW	Arm cavity (f1)	25 mW	Arm cavity (f2)	27 mW
PRC (carrier)	515 W	PRC (f1)	7.3 W	PRC (f2)	1.8 W
SRC (carrier)	107 mW	SRC (f1)	3.4 W	SRC (f2)	1.6 nW
SRC (carrier HOM)	230 mW				

Table 4.1: Light power in the various parts of the interferometer: BRSE

entry points of the interferometer to the DARM error signal. The unit may look strange, but it is identical to SNXXX/DARM in [13]. Basically, it is the ratio of the scattered light transfer function and the DARM transfer functions. These numbers are used by the auxiliary optics group to estimate the scattered light noise.

4.4.1 Light power in the interferometer

It is necessary for the estimation of scattered light noises to know the power of the light fields in the interferometer, because those numbers are the starting point of the scattered light noise calculation. Table 4.1 and Table 4.2 show the light power in the various parts of the interferometer. Most of the values were calculated by the Optickle model, while the higher order mode power was calculated using Finesse, assuming ±1 % differential ROC error of the arm cavity mirrors.

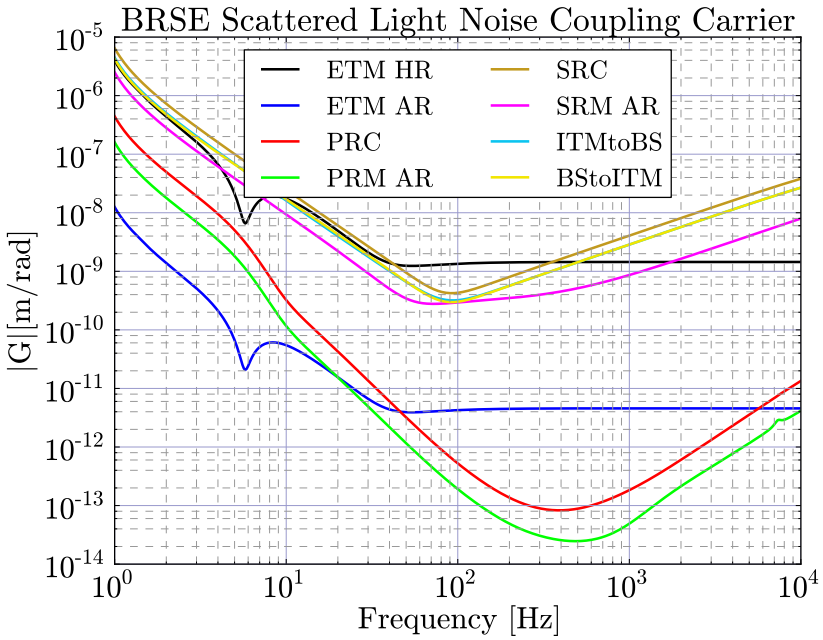

Figure 4.20: Coupling coeffcients of scattered light for the carrier: BRSE

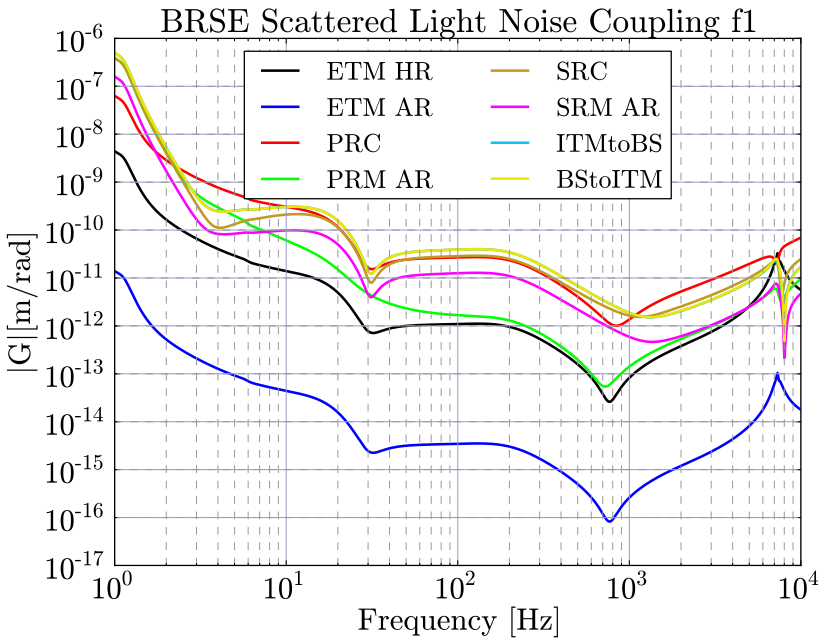

Figure 4.21: Coupling coeffcients of scattered light for the f1 RFSB: BRSE

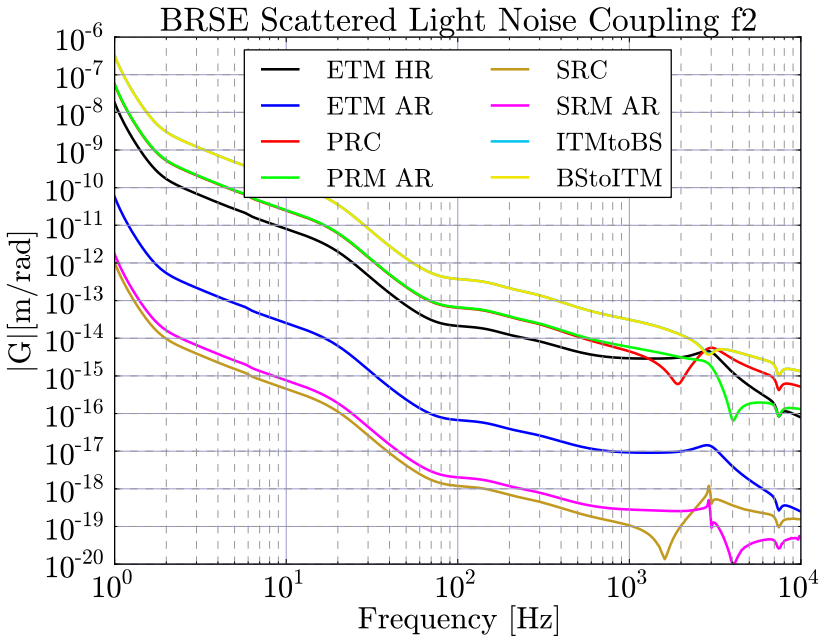

Figure 4.22: Coupling coeffcients of scattered light for the f2 RFSB: BRSE

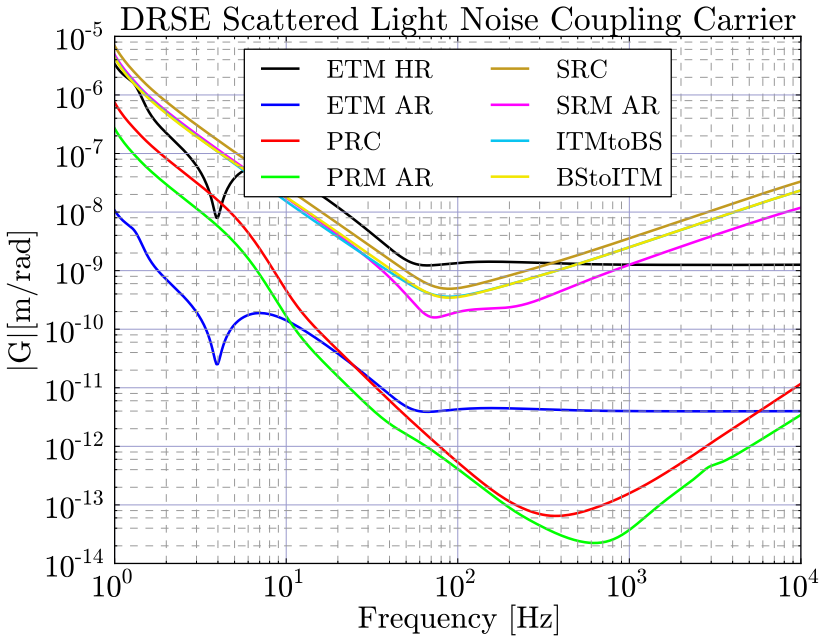

Figure 4.23: Coupling coeffcients of scattered light for the carrier: DRSE

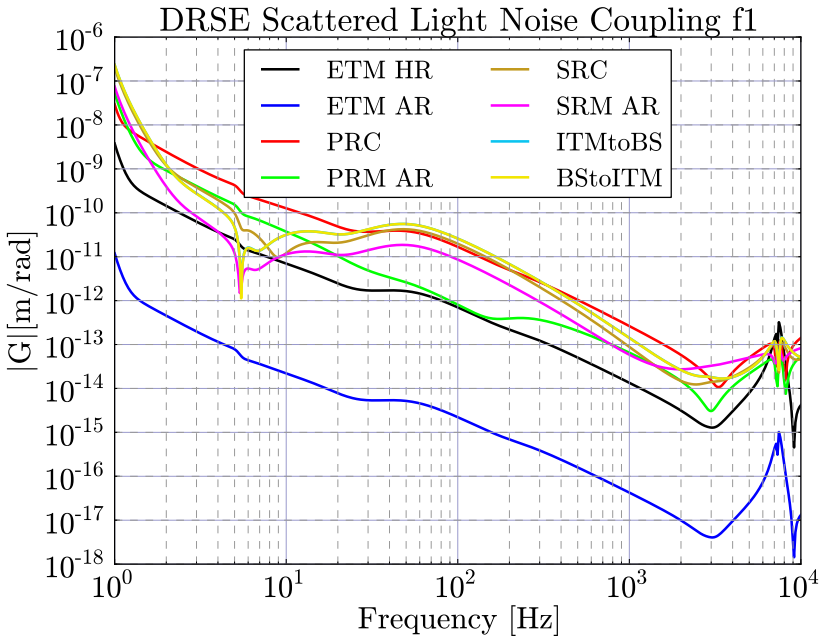

Figure 4.24: Coupling coeffcients of scattered light for the f1 RFSB: DRSE

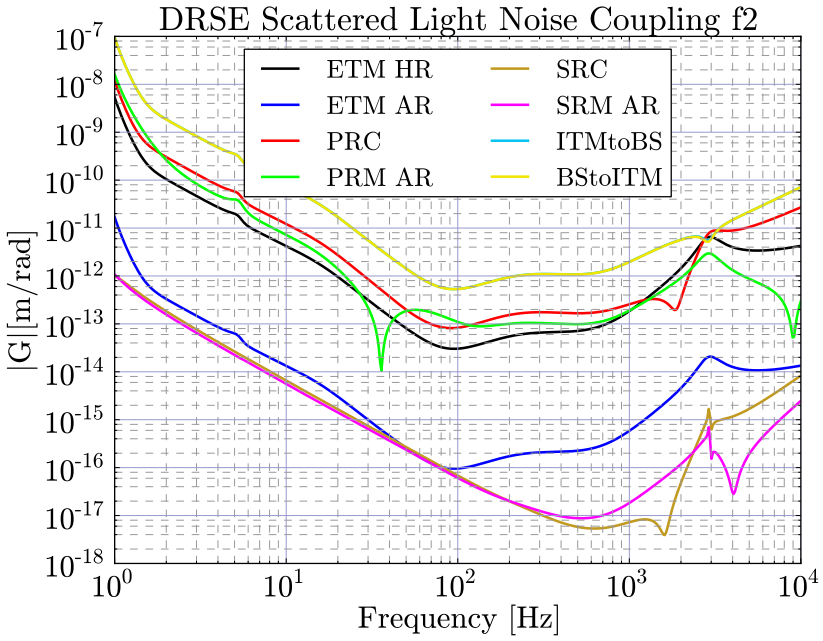

Figure 4.25: Coupling coeffcients of scattered light for the f2 RFSB: DRSE

Arm cavity (carrier)	250 kW	Arm cavity (f1)	20 mW	Arm cavity (f2)	27 mW
PRC (carrier)	515 W	PRC (f1)	5.8 W	PRC (f2)	1.8 W
SRC (carrier)	60 mW	SRC (f1)	2.7 W	SRC (f2)	1.6 nW
SRC (carrier HOM)	230 mW				

Table 4.2: Light power in the various parts of the interferometer: DRSE

Chapter 5

Alignment Sensing and Control Scheme

5.1 Overview

The alignment sensing and control (ASC) scheme of bKAGRA has not yet fully determined. We plan to use a combination of the wave front sensing (WFS) scheme and optical levers. Currently, we have almost finished studying the WFS part with an Optickle model.

5.2 Soft and Hard Modes

The most important thing we have to consider about when designing ASC scheme is the radiation pressure effect. The angular motion of one mirror makes other mirrors to move due to opto-mechanical coupling. Especially, the high circulating power inside the arm cavity (∼380 kW) introduces strong coupling between angular motions of ITM and ETM. So, in order to make it easier to diagonalize the sensing matrix, the WFS signals are sensed in the soft-hard mode basis [5].

The soft mode is the mode which two cavity mirrors tilt antisymmetrically and the radiation pressure torque makes the pendulum mode of the test masses less stiff. The hard mode is symmetric mode and the radiation pressure torque makes the pendulum mode stiffer. The opto-mechanical transferfunctions of the test masses are shown in Figure 5.1. Note that soft mode of yaw motion is unstable(the phase at DC is -180 deg).

In order to estimate how radiation pressure shifts the resonant frequencies, we first fit the transfer function with a simple pendulum transfer function. From the fitting, an equivalent momentum of inertia ($I_{\rm eq}$) and a mechanical restoring torque ($k_{\rm mech}$) is calculated. The soft and hard mode resonant frequencies can be computed by

$$f = \frac{1}{2\pi}\sqrt{\frac{k_{\rm mech} + k_{\rm opt}}{I_{\rm eq}}}, \tag{5.1}$$

where $k_{\rm opt}$ is the radiation pressure torque. $k_{\rm opt}$ of the soft(hard) mode is negative(positive) and the combination of $k_{\rm opt}$ differ by the g-factors and the intra-cavity power. When $k_{\rm mech} + k_{\rm opt} < 0$, resonant frequency is imaginary and angular motion is unstable. Resonant frequencies of the soft and hard modes for negative and positive g-factor are listed in Table 5.1. As you can see from the table, the resonant frequency of the yaw soft mode will be too unstable for the positive g-factors. The pitch soft mode will also be unstable if mechanical restoring torque differed $\sim 30\%$ from the suspension model.

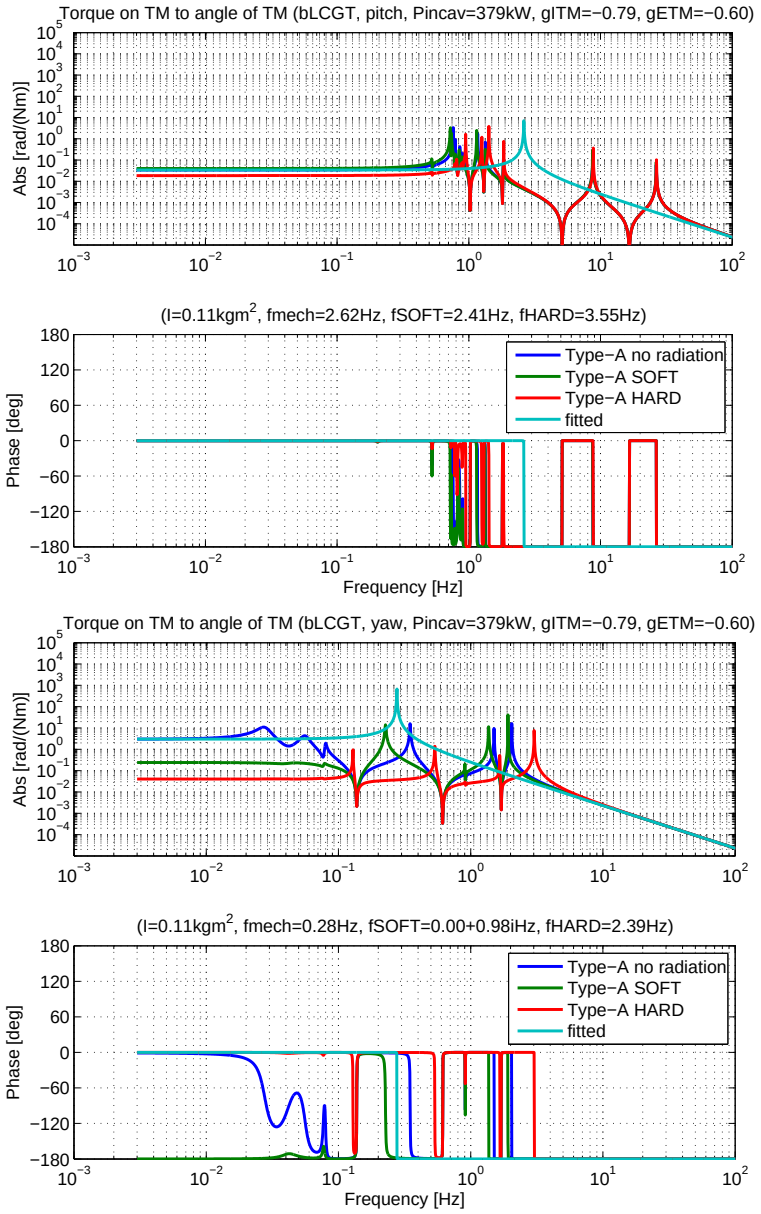

Figure 5.1: The transfer functions from the torque on the test mass to angle of the test mass(top: pitch, lower: yaw). The blue curve shows the mechanical transfer function in the absence of radiation pressure. The green and red curve show the opto-mechanical transfer functions of the soft mode and hard mode.

g-factor	P_{incav} [kW]	pitch [Hz]			yaw [Hz]		
		f_{mech}	f_{SOFT}	f_{HARD}	f_{mech}	f_{SOFT}	f_{HARD}
negative	250	2.62	2.49	3.26	0.28	$0.78i$	1.95
	380		2.41	3.55		$0.98i$	2.40
positive	250		1.77	2.75		$1.90i$	0.87
	380		1.08	2.81		$2.36i$	1.05

Table 5.1: Resonant frequencies under radiation pressure. i represents the instability.

The strategy for the ASC scheme is to make the UGF of the control loop as low as possible ($< 10\,\mathrm{Hz}$) in order not to introduce the WFS shot noise. However, if the unstable frequency is high, we have to make the UGF higher than that frequency to make it stable. This is the main reason why we didn't selected the positive g-factors.

5.3 Simulation Conditions

The simulations of the interferometer response including radiation pressure effects are done using Optickle. This simulation is done for the negative g-factors of the arm cavities.

Arm Cavity Asymmetry

The Optickle model used for ASC simulation doesn't include the arm cavity asymmetry for the simplicity. The two arm cavities are completely identical and the DC power at AS port is completely dark. So, the shot noise estimation for AS port is optimistic.

QPD

By inserting attenuators, the power impinging upon each QPD is adjusted to $\sim 50\,\mathrm{mW}$, except for the AS port.

5.4 Signal Extraction Ports

The signal extraction ports are basically the same as the LSC scheme, but we also use the arm transmitted ports (TRX and TRY). For each port, two QPDs are placed at different Gouy phases. The suffixes used to identify the two are "A" and "B".

The sensing matrix is shown in Figure 5.2. CS, CH, DS and DH in the sensing matrix mean, "Common Soft", "Common Hard", "Differential Soft" and "Differential Hard" respectively. The Gouy phases are optimized to minimize the degeneracy of the signals.

There is no good WFS sensing port for SR2, so the angular motions of SR2 should be controlled by using an optical lever. Since the local control is not included in our model right now, SR2 isn't controlled at all in the following results.

5.5 Angular noise coupling to DARM

5.5.1 Structure of the ASC model

The structure of the ASC model is summerized in Figure 5.3. Notes on the each matrix are the following;

Normalized WFS Sensing Matrix

(Gouy phases at POP A:−68.0, POP B:−61.4 REFL A:88.6, REFL B:−1.4, AS A:88.3, AS B:68.3, TR A:−64.1 deg)

	CS	CH	DS	DH	BS	PR3	PR2	PRM	SR3	SR2	SRM
TRX_ADC	1.00	0.00	1.00	0.00	0.00	0.00	0.00	0.00	−0.00	−0.00	−0.00
REFL_A1I	0.20	1.00	0.00	0.00	−0.00	−0.01	−0.00	−0.01	−0.00	−0.00	−0.00
TRY_ADC	−1.00	−0.00	1.00	0.00	−0.00	−0.00	−0.00	−0.00	−0.00	−0.00	−0.00
AS_A1Q	0.00	0.00	0.20	1.00	0.00	−0.00	−0.00	−0.00	0.00	0.00	0.00
POP_A1Q	0.04	−0.05	1.49	−1.37	1.00	−0.02	−0.00	−0.00	−0.06	−0.01	−0.00
POP_A2Q	−0.65	−0.15	0.00	−0.00	0.35	1.00	0.11	0.05	−0.00	−0.00	−0.00
POP_ADC	−0.15	−0.02	−0.00	0.00	0.09	0.24	1.00	0.42	−0.00	−0.00	−0.00
REFL_B1I	0.53	−0.03	0.00	−0.00	−0.21	−0.71	−0.08	1.00	−0.14	−0.02	−0.01
POP_B1I	−0.97	0.00	−0.03	0.03	−0.17	0.55	0.06	−0.06	1.00	0.11	0.05
AS_BDC	−0.01	0.01	0.36	−0.17	−1.44	−2.34	−0.28	1.93	2.35	0.28	1.00

Figure 5.2: Normalized WFS sensing matrix. Each row is normalized by the diagonal element. SR2 is not controlled by the WFS.

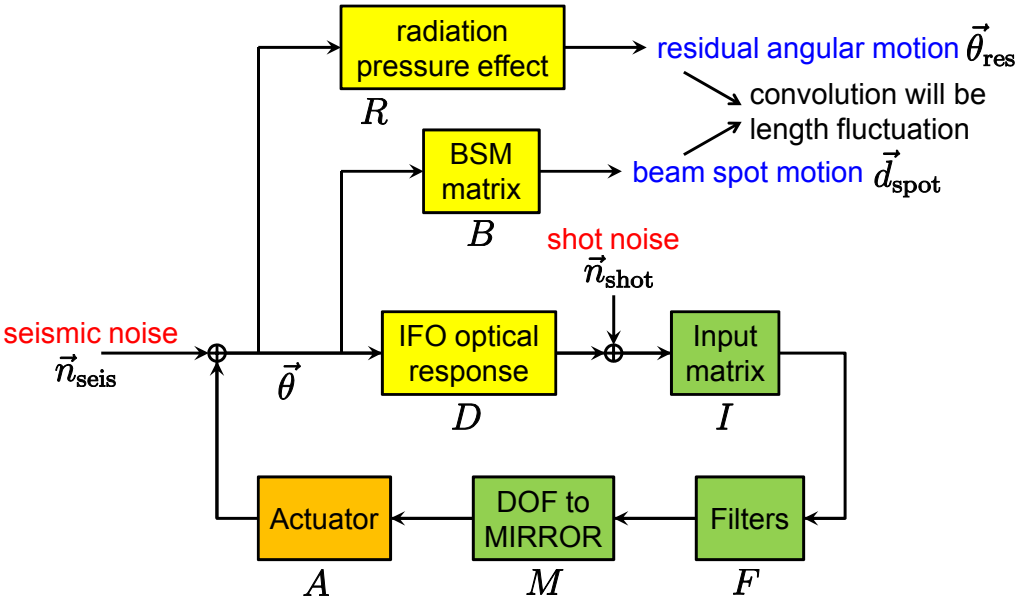

Figure 5.3: Structure of the ASC model.

- IFO optical response D [W/rad] represents the amount of the signal from each mirror at each probe. D is calculated by Optickle simulation (sigAC in Optickle) and it includes the radiation pressure effects.
- Input matrix I is for reconstructing the error signals of the control DOFs. I is ideally computed by taking an inverse of the sensing matrix, but the complete sensing matrix cannot be obtained during the lock aquisition phase. So, in the simulation, we only used large elements in the sensing matrix to compute I.
- Filter F is diagonal filter matrix for each DOF.
- DOF to MIRROR M is the base transformation matrix from DOFs to mirrors.
- Actuator A [rad/Nm] is diagonal actuator matrix for each mirorrs. Actuator transfer functions are calculated by VIS group and currently we are considering only of actuation from recoil masses.
- Radiation pressure effect M [rad/rad] is calculated by Optickle simulation (mMech in Optickle). M is the transfer function matrix from each mirror motion to each mirror motion and it represents the opto-mechanical coupling of the mirrors.
- Beamspot motion (BSM) matrix B [m/rad] is also calculated by Optickle simulation. B is the transfer function matrix from each mirror motion to beamspot motion on each mirror.
- Seismic noise $\vec{n}_{\rm seis}$ [rad] is the angular motion of each mirror caused by the seismic noise and is calculated by VIS group.
- Shot noise $\vec{n}_{\rm shot}$ [W] is calculated by DC power on each QPD. We are assuming the limiting noise of each sensor is shot noise.

By using these matrices, residual angular motion and beamspot motion can be written as,

$$\vec{\theta}_{\rm res} = R(1+G_{\rm mirror})^{-1}(\vec{n}_{\rm seis}+G_{\rm mirror}D^{-1}\vec{n}_{\rm shot}), \tag{5.2}$$

$$\vec{d}_{\rm spot} = B(1+G_{\rm mirror})^{-1}(\vec{n}_{\rm seis}+G_{\rm mirror}D^{-1}\vec{n}_{\rm shot}), \tag{5.3}$$

where

$$G_{\rm mirorrs} = AMFID. \tag{5.4}$$

The cavity length change caused by angular mirror motion is the product of the beamspot displacement and the mirror angle. In the frequency domain, this will be a convolution of the two spectra,

$$\delta L(f) = d_{\rm spot}(f) * \theta_{\rm res}(f) \tag{5.5}$$

$$\simeq d^{\rm RMS}_{\rm spot}\theta_{\rm res}(f) + \theta^{\rm RMS}_{\rm res} d_{\rm spot}(f). \tag{5.6}$$

For the test masses, the length change produced by the angular motion directly couples to DARM. For BS and recycling cavity mirrors, we assumed the coupling factor of $\pi/(2F)$ and 1/100 respectively.

5.5.2 Simulation results

The angular noise coupling to DARM is calculated using the formula presented above. We designed the servo filters to meet the sensitivity. Basically, lower UGF gives lower angular noise coupling at frequencies > 10 Hz. But for the test mass yaw motion, we have to make the UGF at around 3 Hz in order to overcome the radiation pressure antispring. So, we put some extra gain at 0.04-0.05 Hz where there is a seismic noise peak to reduce the RMS of the beamspot motion. The UGFs of the servo loops are listed in Table 5.2.

Figure 5.4 shows the angular noise coupling of each mirror to DARM. They are below the DARM noise (bKAGRA design sensitivity) at frequencies > 10 Hz.

	pitch	yaw
CS, CH, DS, DH	0.06 Hz	3 Hz
other DOFs	0.1 Hz	0.1 Hz

Table 5.2: ASC control loop UGFs

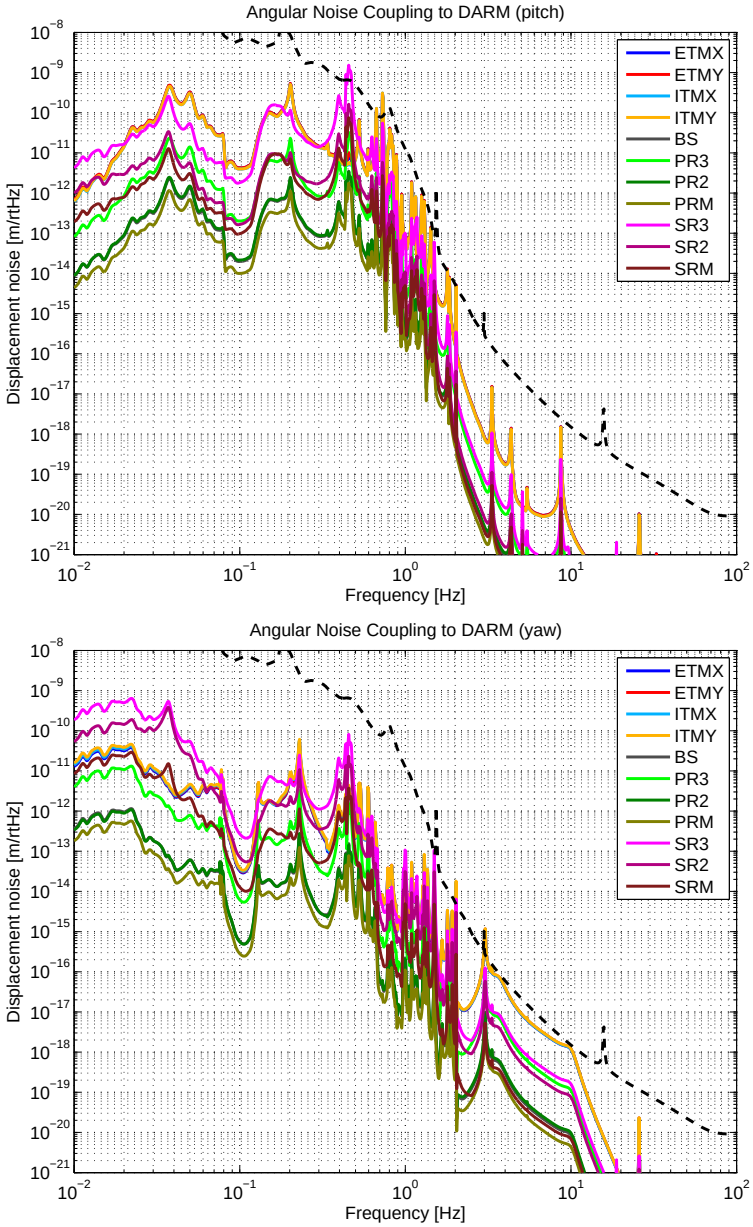

Figure 5.4: Angular noise coupling to DARM (top: pitch, lower: yaw). The dotted line shows bKAGRA design sensitivity.

Chapter 6

Lock Acquisition Scheme

6.1 Overview

Quick and robust lock acquisition is important for maintaining high duty factor. The lock acquisition procedure of bKAGRA proposed here consists of three stages. First, the arm cavities are locked by green lasers at off-resonant positions for the main laser carrier. Then the central part of the interferometer is locked either by using the third harmonics demodulation signals or non-resonant sideband. Finally, the arm cavities are brought to full resonance to the main laser by changing the relative frequency of the green lasers to the main laser. After all the degrees of freedom are brought to the operation points, the error signals are switched to the ones with good shot noise.

The control signals for the central part can be disturbed by the arm cavities if one of the RF sidebands accidentally resonates in the arm cavities. Free hanging mirrors of the arm cavities move around and randomly pass by the resonances of the RF sidebands. This makes the lock acquisition very difficult and a non-deterministic process. For this reason, we will pre-lock the arm cavities at a off-resonant position. The pre-lock position is off-resonant to the carrier because if pre-locked at the full resonance, a huge increase of the carrier power induces a radiation pressure thrust to the mirrors when the PRC is locked. To avoid this shock, the arms are first locked to off-resonance.

After locking the central part, the arm offset is slowly reduced to bring them to the full resonance. During this process, the error signals to lock the central part may be affected. Especially, the single demodulation signals are strongly affected by the large change of the carrier power and phase. Therefore, these signals are not suitable for the lock acquisition. We will use either the third harmonics demodulation signals or the double-demodulation signals with NRS for the lock of the central part during the lock acquisition.

6.2 Green Laser Pre-Lock

6.2.1 Overview

In order to lock the arms at off-resonance of the carrier, we will use phase locked green lasers. Two frequency doubled 532 nm lasers are used. The seed lasers (1064 nm) for those green lasers are phase locked to the main laser carrier with a PLL. Using this PLL, we can sweep the relative frequency of the green lasers to the main laser.

The arm cavity mirrors are dichroic coated to have some reflectivities to 532 nm, forming a low finesse cavity. Each arm cavity is locked to a green laser by the usual PDH scheme. By sweeping the

green laser frequency relative to the main laser, the resonant condition of the arm cavities to the main carrier can be changed smoothly.

The injection points of the green lasers are shown in Figure 6.1. The green laser beams are injected from the back of PR2 (for X-arm) and SR2 (for Y-arm). PR2 is chosen over PR3 because the beam size at PR2 is about 4 mm, which is more manageable compared to 3.5 cm at PR3.

PR2 and PR3 are dichroic coated to have a good transmittance to 532 nm. PR3 and SR3 should have high reflectivities to the green beam, whereas BS should have a high transmittance. Therefore, the beam injected from PR2 mainly reaches the X-arm and the one from SR2 sees only the Y-arm. Of course, the beam separation is not perfect, especially considering that it is difficult to put high spec coatings for 532 nm keeping the coating performance for 1064 nm. Since we do not want to compromise on the performance of the coatings for 1064 nm, we relaxed the requirements for 532 nm, so that the coating company can optimize the coatings mainly for 1064 nm. The problem of the mixture of the light coming back from X-arm and Y-arm can be mitigated by frequency shifting the two green lasers by 100 MHz or so.

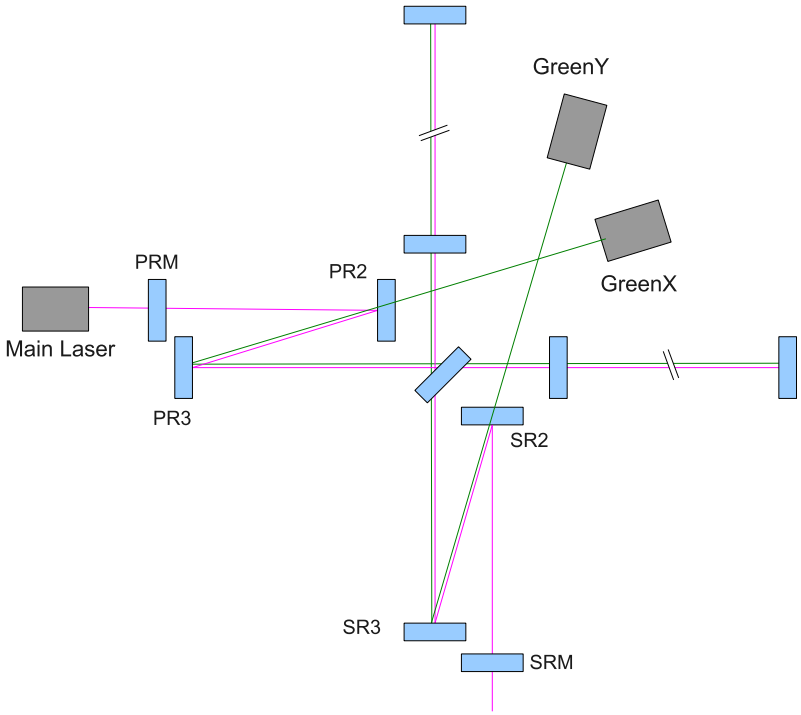

Figure 6.1: Conceptual configuration of the green laser pre-lock. Green lasers are injected from the back of PR2 and SR2. Two green lasers are phase locked to the main laser with a frequency offset of about 100 MHz.

6.2.2 Noise Analysis

In order to keep the arm cavities queiet enough so that they can be brought to the full resonances, the relative fluctuations of the main laser frequency and the arm cavities have to be much smaller than the line width of the arm cavities. Since CARM has two cavity poles, by the PRC and the ACs, the line

width is very narrow (about 1 Hz). If we require the ACs effective length fluctuation, seen from the main laser, to be 1/100 of the resonance width, the RMS length fluctuations of ACs have to be kept smaller than 0.33 pm. The green lock system has to be able to pre-lock the ACs with this stability. In order to design such a system, a noise analysis of the green laser lock system was performed [14]. It was found that the most stringent requirement is imposed on the main laser frequency noise out of the MC.

6.2.3 Third Harmonics Demodulation

One way to get error signals of the central part insensitive to the arm resonance is a method called third harmonics demodulation (THD). In this scheme the REFL port signal is demodulated at the third harmonics frequencies of the RF sidebands. The signal is produced by the beat between the second harmonics of the upper (lower) RF sideband and the first order lower (upper) RF sideband. Since both sidebands are not resonant to the arm cavities, when arm cavities are sufficiently close to the carrier resonance, these sidebands are not affected by the arm cavity motion.

Although the first and second harmonics of the RF sidebands are not resonant to the arm cavity, there is a contribution from the the third harmonics of the RF sideband to the THD signal. This is a beat between the carrier and the third harmonics of the RF sideband. Therefore, there is still inevitable coupling of CARM and DARM motion to the THD signals.

Figures 6.2 to 6.4 show the error signals of the central part plotted by varying the CARM offset from 2 nm to 0. The signals are almost insensitive to the CARM offset. However, MICH signal is largely affected by CARM when the offset is close to zero.

Because of the susceptibility of the MICH signal to the CARM offset, THD is not the default lock acquisition scheme of KAGRA. However, an advantage of THD is its simplicity. No additional modulator or Mach-Zehnder is necessary. We can try it by just adding PDs capable of detecting the third order harmonics. The PD for $3 \times f2 = 135$ MHz may be challenging. However, since this PD is used only for lock acquisition, the noise requirement is not severe.

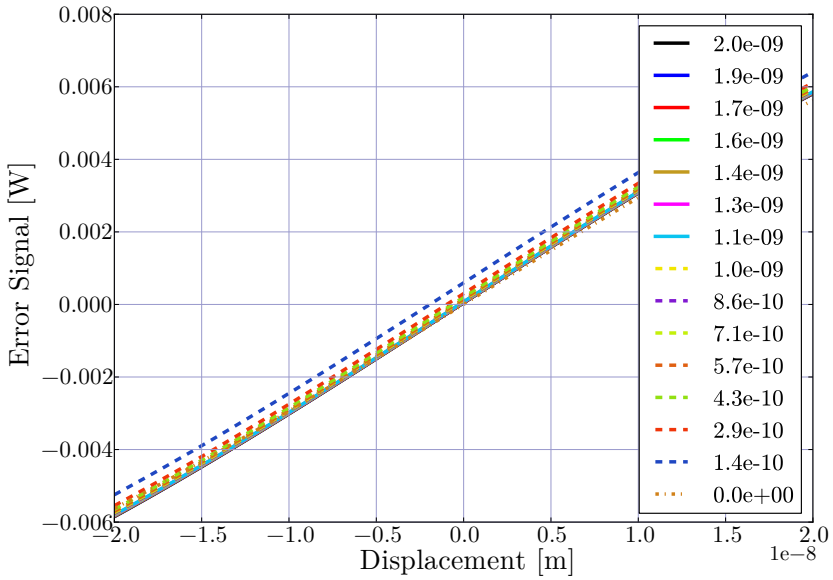

Figure 6.2: THD MICH error signal with various CARM offset. Signal port is REFL, demodulated at $3 \times f1$ in Q-phase.

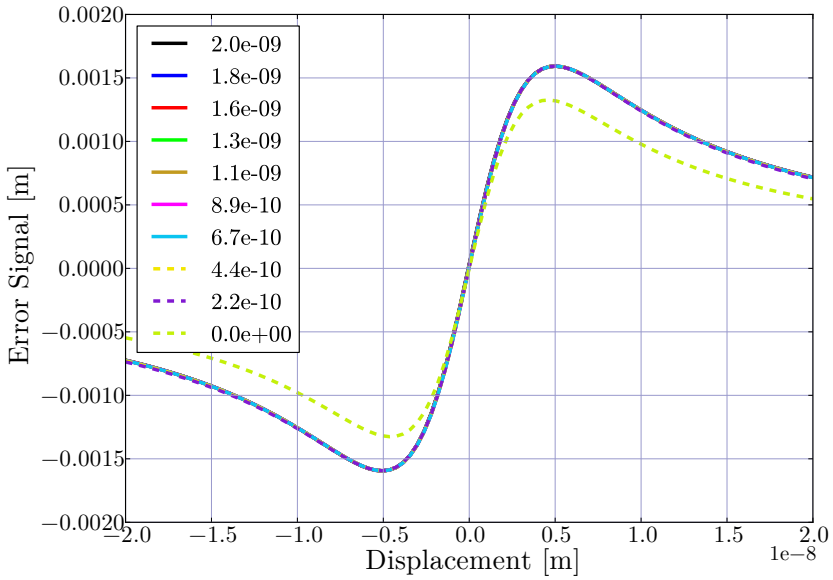

Figure 6.3: THD PRCL error signal with various CARM offset. Signal port is REFL, demodulated at $3 \times f2$ in I-phase.

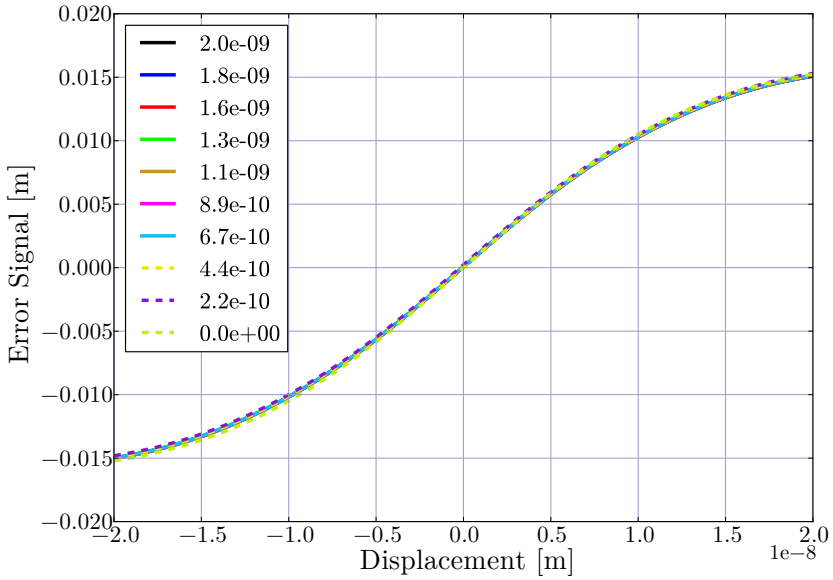

Figure 6.4: THD SRCL error signal with various CARM offset. Signal port is REFL, demodulated at $3 \times f1$ in I-phase.

6.3 Non-Resonant Sideband for Lock Acquisition

Another way to produce robust signals for the central part during lock acquisition is the use of a non-resonant sideband (NRS). The NRS is chosen not to be resonant to any part of the interferometer. So it serves as a stable local oscillator for signal generation.

The NRS error signals of the central part with changing CARM offset are shown in Figures 6.5 to 6.7. As expected, the signals are not affected by CARM at all. We used $f3 = 7 \times f_{\mathrm{MC}}$ as the NRS frequency for those plots.

The NRS scheme requires additional AM modulator to be introduced in the modulation stage. To avoid the generation of sub-sidebands, which interferes with the double demodulation, we also have to use a Mach-Zehnder to separate the AM path from the PM. This is a disadvantage of the NRS method. Since the NRS is only used in the lock acquisition phase, we do not need a large AM. We may also be able to close the AM path after the interferometer is locked, so that the Mach-Zehnder may not introduce excess noise to the laser.

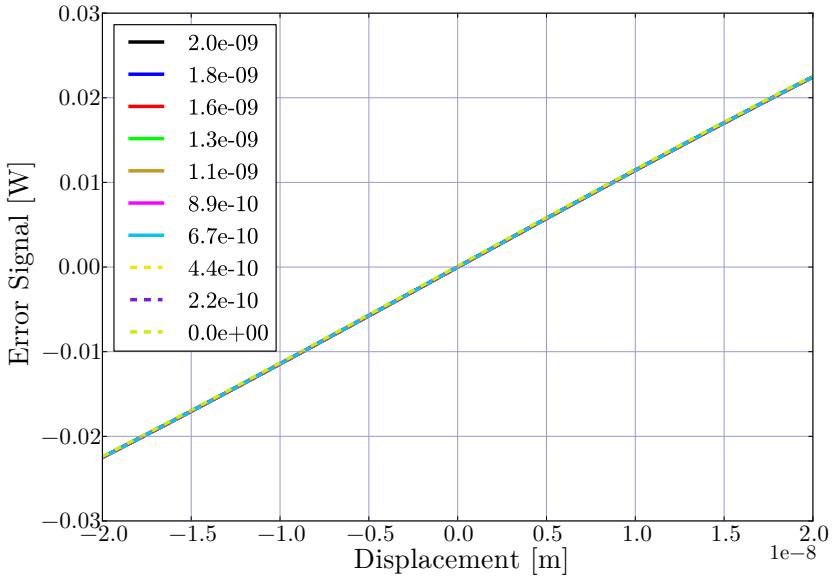

Figure 6.5: NRS MICH error signal with various CARM offset. Signal port is REFL, demodulated at $|f3 - f1|$ in Q-phase.

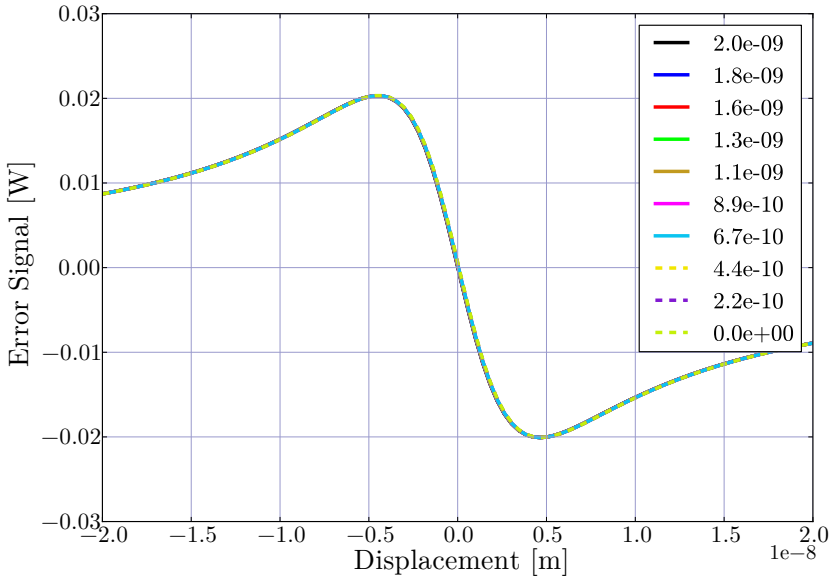

Figure 6.6: NRS PRCL error signal with various CARM offset. Signal port is REFL, demodulated at $|f3 - f2|$ in I-phase.

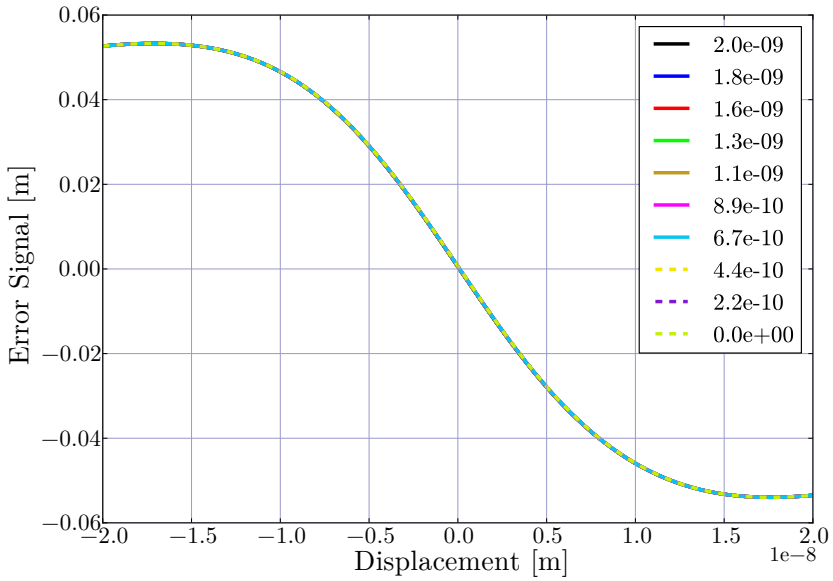

Figure 6.7: NRS SRCL error signal with various CARM offset. Signal port is REFL, demodulated at $|f3 - f1|$ in I-phase.

Chapter 7

Optical Layout

7.1 Basic design

The exact locations and the orientations of the interferometer mirrors have to be determined to satisfy the following criteria:

- X-arm and Y-arm are orthogonal.
- Beams hit the mirrors at the center.
- Recycling cavity lengths and the Schnupp asymmetry match the designed values including the optical distance of the transmissive optics.

Since some optics have AR wedge, it is not a trivial task to trace the beams through the interferometer and find a configuration which satisfy the above conditions. Doing it manually is also an error-prone process. We also have to track unwanted reflections from the AR surfaces to appropriately damp the stray beams. This is also a daunting task. Therefore, we developed a Python library, called gtrace, for tracing beam paths and the evolution of Gaussian beam parameters through the interferometer. Detailed optical layout of KAGRA main interferometer is automatically generated by a Python code given a set of interferometer parameters (distance between the mirrors, mirror properties etc) and constraints.

The optical layout generation code and the generated CAD files are available in the KAGRA svn [7].

7.2 Wedge angle error tolerance

If the wedge angles of transmissive optics, i.e. BS and ITMs, are different from their designed values, the beams do not propagate properly in the interferometer. We have to compensate for the error by tweaking the position and angle of the BS and ITMs. With the SASs, we can move these mirrors by a few mm without opening the vacuum. From this, we can set requirements to the wedge angle error [15]. The conclusion is that in order to make the required amount of adjustment to the positions of the BS and ITMs less than a few mm, the error tolerance has to be about $\pm 1\%$.

7.3 Tunnel Slope

One thing to be kept in mind here is the tunnel slope. Since the 3 km tunnels of KAGRA are slightly tilted for water drainage, the two arms are not on a level plane. We decided that all the main interferometer optics be placed on the plane defined by the two arms. This plane is tilted with respect to the

local gravitationally level plane. The optical layout generated by the above code is drawn on this tilted plane. In the actual construction and the installation of the vacuum chambers, the optical layout has to be projected from the tilted plane to the reference plane used for the construction.

Chapter 8

Installation/Adjustment Procedure

The physical installation of the main interferometer components will be done by other subsystems, such as suspension and mirror. After the initial installation of the mirrors, the distance between them (arm length, PRCL, SRCL, Schnupp asymmetry) have to be checked.

The cavity lengths are checked by measuring the FSR of the cavities. The Schnupp asymmetry can be measured by locking the arms one by one using the REFL port PDH signal, and measuring the difference of the optimal demodulation phases. The g-factor of the arm cavities can be measured by injecting a slightly mis-aligned secondary laser and check the frequency separation between resonances of the TEM00 mode and the TEM10 or TEM01 modes. The finesse of the arm cavities must also be measured.

After those measurements, the MC length should be fine adjusted to set the RF sideband frequencies at a desirable location in the FSR of the arm cavities. Then the length of PRC and SRC will be adjusted to resonate these sidebands. The ROC error of the PR3 (SR3) also has to be compensated by adjusting the distance between PR2 and PR3 (SR2 and SR3), keeping the overall PRC (SRC) length the same [16].

Commissioning is almost a synonym of adjustments to the interferometer. Therefore, the whole commissioning process is the adjustment process.

Chapter 9

iKAGRA

9.1 Overview

iKAGRA is the first milestone of the two phase development of the KAGRA interferometer. The optical configuration of iKAGRA is a Fabry-Perot Michelson interferometer. It will be operated at room temperature and the test mass substrate will be fused silica.

The main purpose of iKAGRA is to *operate a large interferometer as soon as possible to identify potential problems associated with the fascilities and other components in common with bKAGRA*, so that we can take earlier actions to address the discovered issues before starting the bKAGRA commissioning. For this reason, there is no target sensitivity for iKAGRA. The focus is on locking and stably operating the interferometer.

9.2 Changes from bKAGRA

9.2.1 Mirrors

The test masses of iKAGRA will be made of fused silica. The size of the mirrors will be 25 cm diameter and 10 cm thick. The radius of curvatures of the mirrors will be the same as the bKAGRA TMs. Because the index of refraction is different from sapphire, the wedge angle of the iKAGRA ITMs is different from the bKAGRA TMs.

We will continue to use the other mirrors used in iKAGRA through bKAGRA.

9.2.2 Optical Layout

The differences in the optical layout of iKAGRA and bKAGRA are shown in Figure 9.1. The ITMs are moved by 25 m towards ETMs. The ETMs are moved by 35 m towards ITMs. These iKAGRA TMs will be installed in vacuum chambers different from the bKAGRA TMs so that the installation and commissioning of Type-A SAS can be done in parallel with the iKAGRA commissioning. The chambers for iKAGRA TMs will be used as auxiliary optics chamber, for example housing optical lever optics, in bKAGRA.

Because ITM AR surfaces have a finite wedge angle, the beams traveling from the BS to the ITMs are not perfectly orthogonal to each other[1]. Because the ITMs are moved farther away from the BS,

[1] Otherwise, the deflected beam by the AR wedge will not make a normal incidence to the HR surface

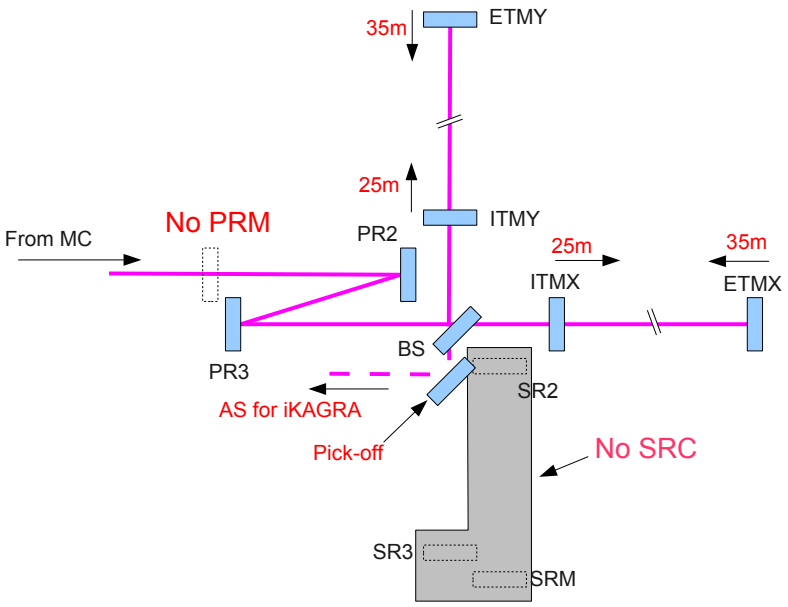

Figure 9.1: Differences between the iKAGRA and bKAGRA optical configurations/layouts.

the beam spot position on the ITMs will be laterally shifted by a few cm. Therefore, the positions of the ITMs will be shifted by the same amount[2].

There are gate valves (GVs) separating the ITM chambers from the 3 km-long vacuum pipes. The initial alignment of the arm cavities will be done while the ITMs are exposed to the air and closing the GVs to keep the vacuum of the long segment. For this purpose, there is an optical window at the center of each GV to allow the beam to pass through. If the lateral shift of the ITMs is too large, the beam will not go through the optical window. In this case, we will move the pipe segments containing the GVs by the same amount to center the beams on the windows. This will be done by preparing two sets of anchor points for the necessary segments of the vacuum pipes.

The PRM will not be installed in iKAGRA. The folding mirrors, PR2 and PR3 will be installed. The whole SRC will not be used in iKAGRA. The SRC part of the vacuum system will be separated from the rest of the interferometer during iKAGRA. Then the SRC mirrors will be installed during the iKAGRA commissioning. In order to get the AS beam of iKAGRA, a pick off mirror will be installed either in the BS chamber or in a temporary chamber on the AS side of the BS chamber.

9.2.3 Mode Matching

We will use the same input mode-matching telescope (IMMT) both in iKAGRA and bKAGRA[3]. The IMMT will be optimized for bKAGRA. Because the PRM will not be installed in iKAGRA, and the positions of the arm cavities are different from bKAGRA, the mode matching of iKAGRA will be degraded. Figure 9.2 shows the input mode matching of iKAGRA mapped by changing the positions of

[2]Currently, the wedge angle of the ITMs are still being adjusted to ease the handling of stray light. The value of this lateral shift depends on the wedge anlge, but a concrete number is not available yet. Still, we know that this will be a few cm.

[3]Because we are lazy :-)

DARM	AS_1Q
CARM	REFL_1I
MICH	REFL_1Q

Table 9.1: Length sensing ports of iKAGRA

the IMMT mirrors centered around the optimized positions for bKAGRA. It is impossible to recover the mode matching to a very good value, such as 99%, even by moving the mirrors by 40 cm. Therefore, we will not attempt to re-optimize the IMMT. We will use the IMMT as is i.e. optimized for bKAGRA. The mode matching for iKAGRA will be then about 87%. We found it acceptable from the experience of TAMA[4].

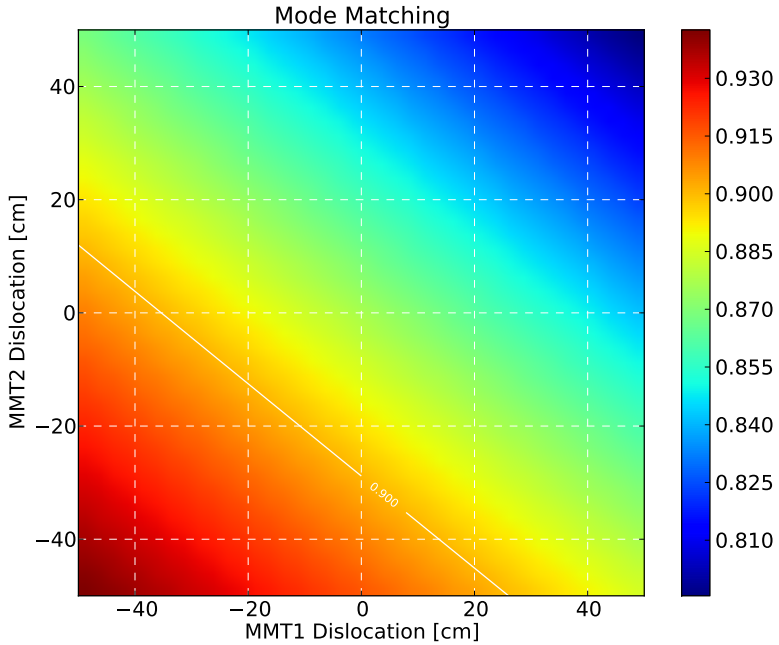

Figure 9.2: Input mode matching of iKAGRA, mapped by changing the positions of the IMMT mirrors from the optimized ones for bKAGRA.

9.2.4 Interferometer Control

We will use only the f1 sideband for the length control of iKAGRA. WFS will not be used, although the installation of hardware and some tests may be performed.

There are three DOFs to be controlled in length. Sensing ports are listed in Table 9.1

There is no plan to use green lock system for iKAGRA. However, we will try to install it as soon as possible. Therefore, the hardware may be installed during iKAGRA phase.

[4]The IMMT of TAMA, which used infamous off-axis parabolic mirrors, had poor quality. Thus the mode matching we got was something like 95%. 87% is worse than this, but not terribly different.

Appendix A

Recycling Cavity Length Determination Algorithm

To be written.

Appendix B

SRCL non-linearity

To be written.

Appendix C

Mixed PM and AM for f1

To be written.

Appendix D

Terminology

Table D.1: Terminology

AC	Arm Cavity	
AM	Amplitude Modulation	
AS	Anti-symmetric port	
Auxiliary DOF		Length degrees of freedom other than DARM
Canonical DOF	Collective name of DARM, CARM, MICH, PRCL and SRCL	
CARM	Common Arm Length	
DARM	Differential Arm Length	
DOF	Degrees Of Freedom	
MC	Mode Cleaner	
MICH	Michelson Part	L shaped part of the interferometer formed by BS and two ITMs
MZ	Mach-Zehnder	
PM	Phase Modulation	
PD	Photo Diode/Detector	
POP	Pick-off in the Power Recycling Cavity	
POX	Pick-off at the ITMX	
POY	Pick-off at the ITMY	
QPD	Quadrant Photo Diode/Detector	
REFL	Reflection port	
RF SB	RF Sideband	
PRC	Power Recycling Cavity	
PRCL	Power Recycling Cavity Length	
SRC	Signal Recycling Cavity	
SRCL	Signal Recycling Cavity Length	

Appendix E

Contributors

Followings are the people have contributed to the discussion of the main interferometer design.

Yoichi Aso (chair), Kentaro Somiya, Osamu Miyakawa, Yuta Michimura, Kazunori Shibata, Kazuhiro Agatsuma, Erina Nishida, Chen Dan, Daisuke Tatsumi, Tomotada Akutsu, Kiwamu Izumi, Koji Arai, Kazuhiro Yamamoto, Hiroaki Yamamoto, Masaki Ando.

Y. Michimura wrote section 5. All the other sections were written by Y. Aso. K. Somiya and O. Miyakawa were deeply involved in the development of the LSC scheme. The PI calculation was done by K. Shibata with the help of K. Yamamoto. The noise analysis of the green lock system was done by D. Tatsumi and K. Arai. Chen Dan validated the code for the optical layout.

Bibliography

[1] K. Somiya, Study report on the new LCGT setup with 22cm mirrors, JGW-T1100644

[2] K. Somiya, JGW-G1100599

[3] V.B. Braginsky et al., Phys. Lett. A 287, 331 (2001).

[4] K. Shibata, Parametric instability in the bKAGRA, JGW-G1200844

[5] J. A. Sidles and D. Sigg, *Physics Letters A* **354**, 167 (2006).

[6] K. Somiya, JGW-G1200850

[7] https://granite.phys.s.u-tokyo.ac.jp/svn/LCGT/trunk/mif/OptLayout/

[8] M. Evans, LIGO Document T070260.

[9] https://granite.phys.s.u-tokyo.ac.jp/svn/LCGT/trunk/mif/IFOmodel

[10] N. Ohmae, PhD Thesis, University of Tokyo, 2011

[11] K. Somiya and O. Miyakawa, *Applied Optics*, **23** (2010) 4335

[12] For example, see the data sheet of AD829 available at http://www.analog.com/

[13] H. Yamamoto, LIGO Document T060073

[14] D. Tatsumi, JGW-T1200788

[15] Y. Aso, JGW-T1100489

[16] K. Agatsuma, JGW-G1100553